small methods
www.small-methods.com

From Material to Cameras: Low-Dimensional Photodetector Arrays on CMOS

*Samaneh Ansari, Simone Bianconi, Chang-Mo Kang, and Hooman Mohseni**

The last two decades have witnessed a dramatic increase in research on low-dimensional material with exceptional optoelectronic properties. While low-dimensional materials offer exciting new opportunities for imaging, their integration in practical applications has been slow. In fact, most existing reports are based on single-pixel devices that cannot rival the quantity and quality of information provided by massively parallelized mega-pixel imagers based on complementary metal-oxide semiconductor (CMOS) readout electronics. The first goal of this review is to present new opportunities in producing high-resolution cameras using these new materials. New photodetection methods and materials in the field are presented, and the challenges involved in their integration on CMOS chips for making high-resolution cameras are discussed. Practical approaches are then presented to address these challenges and methods to integrate low-dimensional material on CMOS. It is also shown that such integrations could be used for ultra-low noise and massively parallel testing of new material and devices. The second goal of this review is to present the colossal untapped potential of low-dimensional material in enabling the next-generation of low-cost and high-performance cameras. It is proposed that low-dimensional materials have the natural ability to create excellent bio-inspired artificial imaging systems with unique features such as in-pixel computing, multi-band imaging, and curved retinas.

1. Introduction

The invention of semiconductor-based imaging in 1969, recognized by the 2009 Nobel Prize, has revolutionized many aspects of our lives. Today, most mobile phones have at least one CMOS camera, and there are more mobile phones than there are people on the planet.[1] Digital imagers are at the heart of the most advanced instruments humans have made to explore the unknowns of the world, from the smallest particles to the vast of the Universe. While silicon was the first semiconductor used in solid-state imaging, its bandgap prevents imaging beyond a wavelength of ≈1 µm. The demand for imaging at longer wavelengths promoted integration of different semiconductors on silicon and the first infrared focal plane array based on indium bump-bonding was demonstrated as early as 1975.[2] This integration method has remained the standard process for heterogeneous integration of semiconductors on silicon over the past five decades. However, Indium bump-bonding is far from ideal and has led to the high cost and limited resolution of the non-silicon imagers. While significant investments have been made to find better integration methods, such as DARPA's wafer scale infrared detectors, the inherent properties of bulk and epitaxially grown semiconductors have limited their success so far.

Low-dimensional materials, such as nanowires and 2D van der Waal (vdW) materials, have emerged as a promising platform for imaging applications across the electromagnetic spectrum, from X-ray to terahertz (THz) frequencies. These materials possess unique physical properties, such as natural surface termination without dangling bonds, low capacitance, and flexibility. These properties not only offer the possibility of better heterogeneous integration methods, but also other exciting new opportunities that could shape the future of digital imaging. **Figure 1** shows the historical progress in three key metrics of imagers, namely their spatial resolution, spectral diversity, and energy efficiency. While this figure is not meant to present all important parameters, it is evident from this figure that a myriad of commercial and scientific applications has driven the technology to do exceedingly better in their fundamental performance metrics. In this review, we explore methods to harness the unique properties of

S. Ansari, H. Mohseni
Electrical and Computer Engneering Department
Northwestern University
Evanston, IL 60208, USA
E-mail: hmohseni@northwestern.edu

S. Bianconi
Jet Propulsion Laboratory
California Institute of Technology
Pasadena, CA 91109, USA

C.-M. Kang
Photonic Semiconductor Research Center
Korea Photonics Technology Institute
Gwangju 61007, Republic of Korea

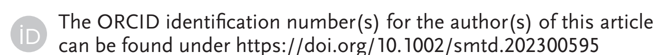

The ORCID identification number(s) for the author(s) of this article can be found under https://doi.org/10.1002/smtd.202300595

© 2023 The Authors. Small Methods published by Wiley-VCH GmbH. This is an open access article under the terms of the Creative Commons Attribution License, which permits use, distribution and reproduction in any medium, provided the original work is properly cited.

DOI: 10.1002/smtd.202300595

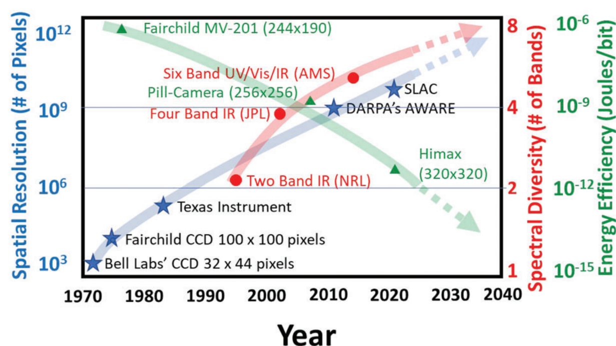

Figure 1. Progress in three key parameters of imaging sensors.

low-dimensional material that could drive the field of imaging in the coming decades. We believe that the most notable impacts include:

1) Low-cost and high-performance cameras across different EM bands: vdW and 2D material can be "stamped" on the silicon electronics (ROIC) to create low-cost solutions with equal or better performance than existing cameras in challenging EM bands such as X-ray, deep UV (DUV), Infrared (IR), and Tera Hertz (THz). Flexible detectors based on 2D material have already been demonstrated at X-ray,[3] DUV,[4,5] IR,[6,7] and THz.[8,9] Such an ability promises Low-cost manufacturing of cameras across a broad range of EM spectrum, due to elimination of the yield-limiting indium bump-bonding. In the following sections, we show that their inherent flexibility allows their bonding to the non-planar surfaces of the existing or future ROICs made by the conventional CMOS fabs, without the need for an intermediate material.
2) Minimal need for surface passivation: vdW material have atomically smooth surfaces with very little dangling bonds[10] Unlike conventional semiconductors, these intrinsically nano-scale materials do not need extensive surface passivation and hence are significantly easier to work with at smaller dimensions. This property reduces the complexity of manufacturing and allows stacking of this material for creation of advanced and/or multi-functional sensors.
3) New functionalities inspired by nature: one of the unique aspects of natural human vision is its extremely high sensitivity, resolution, efficiency, and field of view. Not only the Rod cells in the Human eye can detect a single photon,[11] but their signals are pre-processed by the Ganglion cells, with extremely high energy efficiency and robustness before sent to the brain. While massive research activities have recently been dedicated to mimicking such natural sensors using silicon-based devices,[12] their performance is still far from their biological counterparts. We believe that low-dimensional materials present a unique opportunity to closely mimic biological imaging system, to create a new generation of imaging systems with unparalleled abilities such as:
   a) Ultimate photon sensitivity: it can be shown that the sensitivity of photodetectors, with a large enough internal gain, depends on their internal capacitance.[13] Therefore, reducing the capacitance of such photodetectors can lead to more sensitive devices as shown experimentally.[14,15] The ultimate sensitivity to a single photon emerges as the device capacitance approaches the quantum capacitance of $C_0 = q^2/kT$, where q is the charge of an electron, k is the Boltzmann constant, and T is the temperature. The value of C_0 is quite small at room temperature, so using top-down nano-fabrication methods for making room temperature single-photon detectors is quite challenging. However, low-dimensional materials present an interesting opportunity in making such devices due to their naturally small dimensions and unusually low dielectric constants.[16]
   b) Multi-band imaging: researchers have made significant progress in expanding the spectral imaging range beyond the visible band. One promising avenue of research involves the development of cameras that can detect polarization and more than three colors in the visible band. Inspired by the vision of mantis shrimp, which has seven-color sensors and polarization sensitivity, scientists are exploring manmade versions for better sensing and detection in a range of scenarios.[17,18] A step further would be simultaneous imaging in multiple spectral bands, such as visible, infrared, and THz. Such cameras could provide an unprecedented level of information in a compact and efficient format. Low-dimensional materials are uniquely suitable for creating multi-band cameras, since they are capable of detecting an extremely wide range of EM radiation, from X-rays and DUV to IR and THz. By combining multiple low-dimensional materials, it may be possible to create cameras that can sense multiple wavelengths bands simultaneously. Such cameras would have important applications in fields such as medical imaging, remote sensing, defense, and astronomy.
   c) Passive depth extraction: The retina of jumping spiders (*Salticidae*) is made of stacked translucent retinae to allow the spider to accurately create a 3D depth image.[19] The thin nature and stacking ability of 2D material provides a unique opportunity for making cameras with 3D depth perception. Recently, semi-transparent 2D photodetectors were used for depth perception and integral imaging.[20] Unlike the commonly used active ranging, which requires emission of EM waves, such passive depth imaging methods can be extremely efficient, compact, and without any interference.
   d) Curved image sensors: Advanced eyes in the animal kingdom have curved retinae. Not surprisingly, it can be shown that curved focal plane arrays have a significant advantage compared with the flat ones,[21] as they can reduce the size, complexity, and cost of the optics. This is especially important in the bands where conventional lenses do not work, such as X-ray and DUV. Fortunately, a new method has been developed that allows any commercial silicon CMOS image sensors to be thinned and formed into accurate, highly curved optical surfaces with undiminished functionality.[22] Unfortunately, this method is not compatible with indium bump-bonding and hence not useful in making cameras sensitive to infrared or other bands that need non-silicon material. While it has not been demonstrated yet, we propose that 2D material could be used with curved ROICs to create

© 2023 The Authors. Small Methods published by Wiley-VCH GmbH

23669608, 0, Downloaded from https://onlinelibrary.wiley.com/doi/10.1002/smtd.202300595 by Northwestern University Libraries, Wiley Online Library on [14/11/2023]. See the Terms and Conditions (https://onlinelibrary.wiley.com/terms-and-conditions) on Wiley Online Library for rules of use; OA articles are governed by the applicable Creative Commons License

high-performance and compact cameras at challenging EM bands.

e) In-sensor computing: we know that the human eye not only includes photosensitive cone and rod cells, but also performs massive early computation with another set of cells called Ganglion cells. Their function is to significantly reduce the volume of data without degrading the spatial and temporal resolution of events. This feat is primarily performed through the suppression of unwanted spikes, as originally demonstrated by Torstein Wiesel,[23,24] the 1981 winner of the Nobel prize in medicine. Interestingly, a growing number of reports show that low-dimensional materials have excellent properties for low-energy neuromorphic computing. Implementation of in-sensor computing (a.k.a. "in-pixel computing") could enable imaging with extremely large resolution but low power consumption—with massive impact on many fields, including medicine, high-energy particle physics, and astronomy.

Despite such great potentials, it is instrumental to point out that low-dimensional materials suffer from three major shortcomings, namely:

1) Chemical stability: degradation due to oxidation and similar ambient elements is currently a major issue. One can anticipate that similarly to organic LED (OLED), robust transparent sealing methods will be developed once the commercial demand for the technology grows beyond a certain threshold.
2) Large-area synthesis and transfer: one major breakthrough in 2D material was the discovery of processes for large-area synthesis and transfer of graphene. While a wide range of attractive 2D material exists, not all can be produced with good quality on a large area, and in a way that could be transferred to a receiver substrate.
3) Limited optical absorption: The small volume of low-dimensional material leads to a generally small optical absorption, despite their unusually large optical dipole transitions and joint density of states.[25] While many research groups have demonstrated significant increase in absorption by using optical cavities near a particular wavelength, broadband and near-unity optical absorption have remained elusive.

With these limitations in mind, we review the best existing materials and methods in creating high-resolution and high-performance imaging chips using low-dimensional materials.

2. Imaging with Low-Dimensional Material

For the successful implementation of different photo-sensitive low-dimensional materials into functional imagers, these materials must satisfy several requirements critical for imaging performance, ranging from the optical and electronic properties necessary for effective detection, to the fabrication and reliability considerations.

2.1. Desired Material Properties

2.1.1. Optical

As in previous section, even though light-matter interaction is often enhanced in atomically thin low-dimensional materials, the effective optical absorption is intrinsically lower than that of conventional bulk semiconductors, due to the extremely low thickness of low-dimensional material causing short interaction length with light. This effect can hinder imaging and detection performance metrics, such as quantum efficiency. Some solutions to improve the optical absorption rely on stacking thick layers of low-dimensional materials while maintaining their dimensionality (e.g., solution-dispersed flakes,[26] or dense vertical arraying of nanowires[27]). In addition, photonics solutions discussed in the later sections could be used for a wide range of materials. Moreover, we note that the low optical absorption in low-dimensional photodetectors could be leveraged for advanced functionality such as 3D light field imaging, as will be discussed in the following section. Finally, low-dimensional materials offer unique optical tuning and engineering. One attractive feature of some low-dimensional materials is their bandgap tunability depending on their dimensions, such as thickness for Black Phosphorus or diameter for quantum dots, which enables to design detectors operating across a wide spectral range. Another similarly interesting adjustable feature is their optical birefringence[28] due to their reduced dimensionality.

2.1.2. Electrical

Some electrical characteristics of the photo-sensitive material are also crucial for imager implementation. Typically, good carrier lifetime and mobility favor the transport of photogenerated charges to the electrodes before they can recombine; however, low-dimensional materials have extremely anisotropic mobilities, with in-plane charge transport much more efficient that out-of-plane, which can cause pixel crosstalk in imaging arrays if no electrical isolation is ensured. Finally, the possibility to dope these materials and stack them to form heterojunctions is crucial to enable the design of opto-electronic structures that are optimized for light detection, such as PIN junctions[29] and phototransistors.[20]

2.1.3. Fabrication Compatibility and Chemical Stability

Large-area uniformity is paramount for the fabrication of useful focal plane arrays, and it represents one of the main challenges for the implementation of imagers based on low-dimensional materials. Nonetheless, chemical deposition methods and solution-based processes yielding good uniformity have been developed, enabling the demonstration of an imager based on a deposited film of graphene sensitized by spin-on colloidal quantum dots,[30] showing good large-area uniformity. An additional crucial feature is the compatibility with standard VLSI semiconductor processing techniques, such as photolithography and etching, as discussed in more detail in the following sections. Finally, passivation can also play a significant role in stabilizing and protecting the photo-sensitive materials (see **Table 1**).

© 2023 The Authors. Small Methods published by Wiley-VCH GmbH
23669608, 0, Downloaded from https://onlinelibrary.wiley.com/doi/10.1002/smtd.202300595 by Northwestern University Libraries, Wiley Online Library on [14/11/2023]. See the Terms and Conditions (https://onlinelibrary.wiley.com/terms-and-conditions) on Wiley Online Library for rules of use; OA articles are governed by the applicable Creative Commons License

23669608, 0, Downloaded from https://onlinelibrary.wiley.com/doi/10.1002/smtd.202300595 by Northwestern University Libraries, Wiley Online Library on [14/11/2023]. See the Terms and Conditions (https://onlinelibrary.wiley.com/terms-and-conditions) on Wiley Online Library for rules of use; OA articles are governed by the applicable Creative Commons License

Table 1. Notable low-dimensional materials used for photon detection, and their material properties and performance parameters most relevant to imaging applications.

Material	Dimension	Deposition/transfer	Patterning	Passivation	# of pixels	Advanced functionality	Bandgap [eV]	Ref.
SW CNT	1D	Solution, dry-transfer	Photolithography		1		0.08–2.0	[133]
ZnO nanowires	1D	Low-T epitaxial growth		Selective growth	1		3.26–3.35	[134]
Zn_2SnO_4 nanowires	1D	Growth			1		3.26–3.64	[135]
Ge nanowires	1D	Growth			1		0.8–1.1	[136]
Graphene	2D	Solution, CVD	EBL, dry etching (Oxygen plasma)	Al2O3	1	THz, flexible	0	[9]
MoS_2	2D	Solution, CVD	Aerosol-jet printing, FIB		8×8	Neuromorphic	1.2–1.9	[57,61–62,137]
WSe_2	2D	Solution, CVD			1		1.2–1.65	[138]
WS_2	2D	Solution, CVD			1		1.35–2.0	[139]
Ga_2O_3	2D	Dry-transfer	EBL	h-BN	1	flexible	4.7–4.9	[4]
GaSe	2D	MBE, Dry-transfer	EBL		16×1	multi-spectral	1.53–2.71	[140,33]
ReS_2	2D	Solution, CVD			1		1.35–1.43	[141]
$MoTe_2$	2D	Solution, CVD			1		0.9–1.1	[142]
Black Phosphorus	2D	Solution, Dry-transfer		h-BN	1	multi-spectral, polarizing filter	0.3–2.3	[35–36,38–39]
Te	1D/2D	CVD			1	polarization sensitive	0.33–0.35	[32,31]
Sn-Pb perovskite	2D	Solution		PEIA, C60, BCP	1		1.17–1.55	[143]
CsPbSrBr perovskite	0D	Solution			1	Gamma ray scintillation	2.29–2.64	[144]
PbS CQD + Graphene	OD + 2D	Wet transfer + Colloidal solution	Photolithography	Oleate capping	388×288	broadband	0.56–1.77	[30]

2.2. Unique Capabilities of Low-Dimensional Material for Imaging Beyond CMOS

As mentioned in the previous sections, low-dimensional materials possess a unique set of material properties that makes them promising candidates for advancing imaging performance beyond the current state of the art, based on bulk crystalline materials. **Table 2** summarizes the main capabilities that can be enabled by leveraging low-dimensional materials for imaging and outlines a few applications that can benefit from them. In the following subsections we discuss in detail some of these applications, together with the critical requirements for their implementation using low-dimensional materials.

Table 2. Unique material capabilities of low-dimensional materials and related applications that can potentially benefit from them.

Unique material capability	Applications
Low-dimensionality and low capacitance	High-sensitivity imaging
Fabrication flexibility and transferring	Scalable and low-cost non-visible imagers; Curved imagers
Stackable materials of different bandgaps	Multi-spectral imaging; Broad spectral coverage
Conversion of radiation to visible light	CMOS-based imaging
Neuromorphic electronic properties	In-pixel computation
Intrinsic polarization-sensitivity of materials	Polarimetric imaging
Semi-transparent detectors	Depth extraction and light field imaging

2.2.1. Multi-Spectral Imaging

Thanks to their fabrication flexibility and direct deposition methods, many low-dimensional materials can be combined in a manner that is impossible for conventional crystalline detector materials, which must be lattice-matched in order to avoid excessive defect densities. As a result, low-dimensional materials are uniquely suited for combining several layers of different absorbers within a single device to achieve multi-spectral detection and imaging. In addition, since low-dimensional materials have been demonstrated to cover the bands from X-ray[31] to THz[32] (see **Figure 2**), this represents an opportunity to outperform conventional multi-spectral imagers both in terms of optical bandwidth, as well as number of distinct spectral bands. A significant number of dual-band visible/short-infrared photodetectors[33,31] and focal plane array[34] based on low-dimensional materials have

 © 2023 The Authors. Small Methods published by Wiley-VCH GmbH

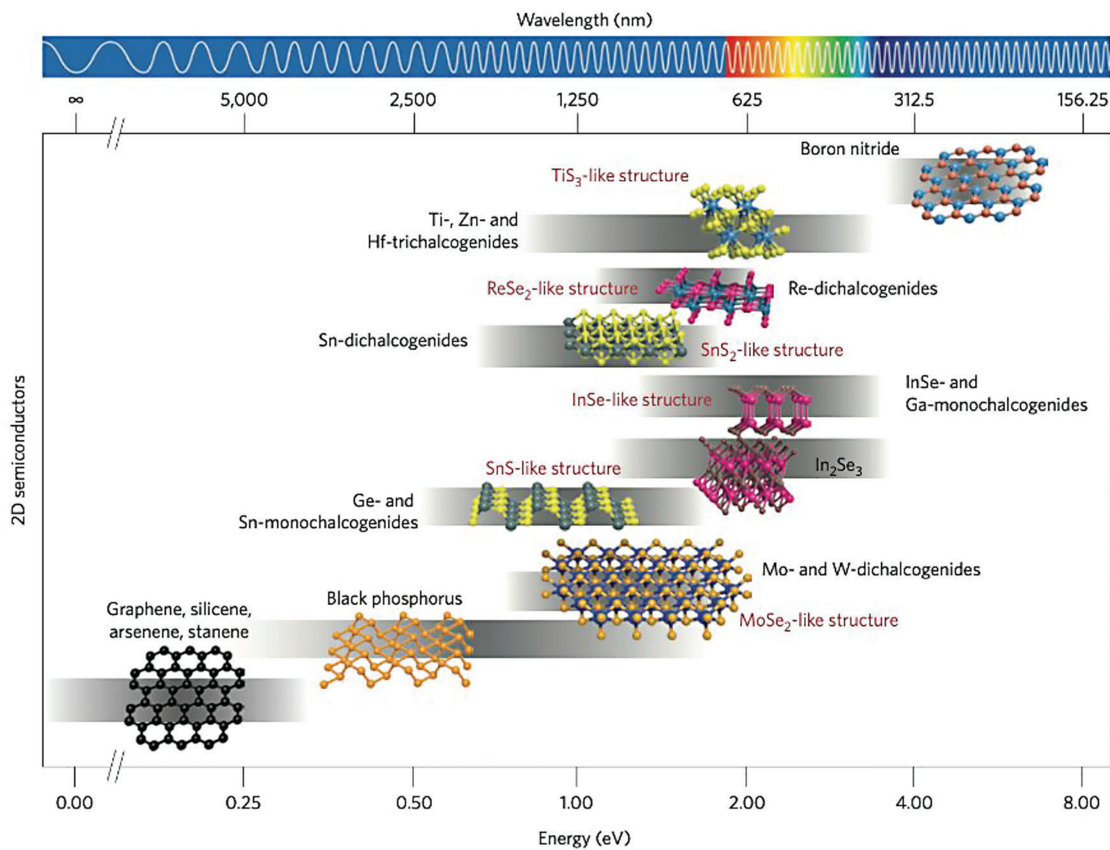

Figure 2. Comparison of the bandgap values of the most common 2D semiconductor material families, as well as a schematic of their crystal structures. Bandgap can be typically tuned by changing the number of layers, straining or alloyed, as displayed in the figure. Reproduced with permission.[37] Copyright 2016, Springer Nature.

been reported. In particular, bias-switchable dual-band detectors such as those shown in **Figure 3**[35] are especially attractive for their ability to achieve multi-spectral imaging without the need for additional components such as spectral filters; however, their integration into focal plane arrays based on conventional readout circuitry will require specialized architectures capable of switching the detector bias during imaging, such as a global transparent contact covering all pixels.[36]

Furthermore, low-dimensional materials have also enabled some exotic detection techniques, based on unique properties of low-dimensional materials, such as plasma-wave THz detectors in Graphene.[35] Some of these novel detection techniques also enable energy-sensitive detection, such as in photo-ring oscillators based on low-dimensional materials.[38]

2.2.2. Conversion to Visible Light

A device concept that has been gaining momentum over recent years is based on converting light of various wavelengths to visible light, which leverages the mature and widely available CMOS imager technology to achieve megapixel imaging. Such photon conversion can be achieved by taking advantage of several different processes:

Scintillation: when the incoming photons possess higher energy than visible ones, scintillation may be used for the

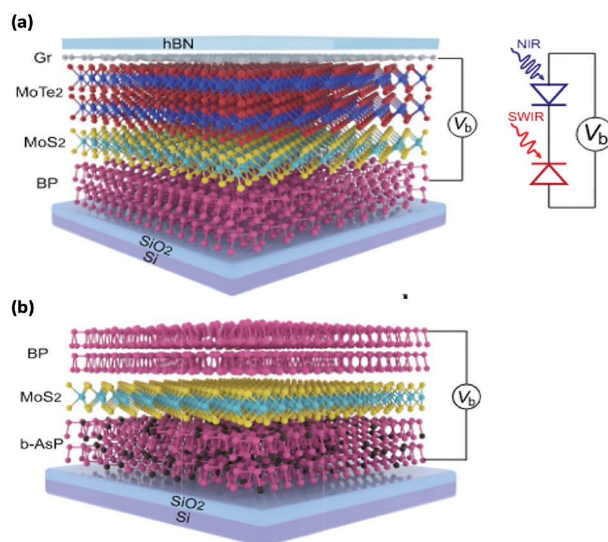

Figure 3. Bias-switchable multi-spectral detectors based on low-dimensional materials such as a) MoS_2, $MoTe_2$ black phosphorus (BP), and b) black arsenic phosphorus (b-AsP). Adapted with permission.[35] Copyright 2022, American Chemical Society.

© 2023 The Authors. Small Methods published by Wiley-VCH GmbH

23669608, 0, Downloaded from https://onlinelibrary.wiley.com/doi/10.1002/smtd.202300595 by Northwestern University Libraries, Wiley Online Library on [14/11/2023]. See the Terms and Conditions (https://onlinelibrary.wiley.com/terms-and-conditions) on Wiley Online Library for rules of use; OA articles are governed by the applicable Creative Commons License

23669608, 0, Downloaded from https://onlinelibrary.wiley.com/doi/10.1002/smtd.202300595 by Northwestern University Libraries, Wiley Online Library on [14/11/2023]. See the Terms and Conditions (https://onlinelibrary.wiley.com/terms-and-conditions) on Wiley Online Library for rules of use; OA articles are governed by the applicable Creative Commons License

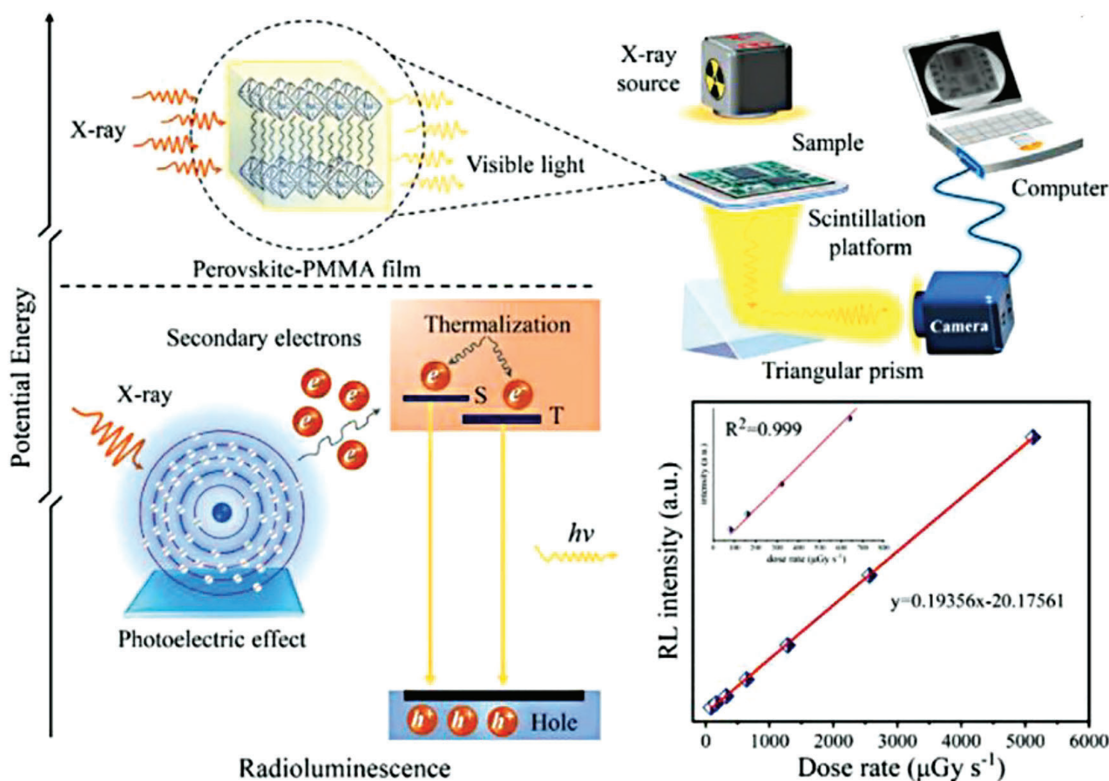

Figure 4. Schematic of a solution-processed metal Halide Perovskite scintillator for X-ray detection using visible CMOS cameras, and the linearity plot of luminescence intensity versus dose rate. Repoduced with permission.[42] Copyright 2020 American Chemical Society.

"down-conversion" of photon frequency. In this process, one high-energy photon is absorbed and then re-emitted in the form of one or more lower energy photons. This method is routinely used for the detection of X-ray and UV photons. In recent years, solution-processed and crystalline perovskite have been reported as excellent materials for scintillators, thanks especially to the ability to load perovskite with molecules and atoms with exceptional photo-sensitive properties.[39,40,41] In particular, scintillators based on solution-processed metal halide perovskites, such as those shown in **Figure 4**, have attracted growing interest thanks to their unmatched absorption and photoluminescence characteristics, together with their ease of fabrication and integration.[42] Notably, metal halide perovskite semiconductors have also demonstrated direct detection of high-energy photons, growing to rival the performance of traditional scintillator counterparts.[43]

Parametric up-conversion: when the incident photons possess lower energy than the visible photons, their "up-conversion" can be achieved by means of parametric conversion in non-linear optical materials, where the additional energy required is provided by a pump beam of light. In recent years, novel low-dimensional materials have been reported with effective third-order non-linearities significantly higher than that of silica fibers traditionally used for up-conversion.[44] Nonetheless, the interaction length required for efficient parametric up-conversion still limits this application to waveguide-based architecture, therefore preventing its implementation on surface-normal imager architectures.

Non-degenerate two-photon absorption: Two-photon absorption is a well-understood process, where two photons with an energy of half of the bandgap of a semiconductor can be absorbed simultaneously to create electron-hole pairs. However, conventional two-photon absorption is extremely inefficient and requires very large photon densities. In contrast, if one of the photons (i.e., pump photon) has an energy close to the bandgap the process can be significantly more efficient. This so-called non-degenerate two-photon absorption has been successfully used to detect photons with energies well below the semiconductor bandgap.[45] Note that unlike parametric down-conversion, phase matching is not required in this approach and hence in-pixel conversion is possible, as recently demonstrated in silicon CMOS imagers.[46] One major issue in this approach is the background noise produced from the conventional two-photon absorption of the pump photons. We speculate that the inherent polarization sensitivity of anisotropic low-dimensional materials[47] could be used to address this limitation and achieve a much lower noise and higher sensitivity.

Electronic up-conversion: perhaps the most promising method for up-conversion-based imaging, is by using electronic amplification in monolithically integrated absorber/emitter structures. In this approach, the incoming photons are absorbed and transformed into electron–hole pairs in a material optically tailored for absorption at the desired wavelength; these photogenerated carriers are then transported to an adjacent layer of the device structure, where they radiatively recombine to emit light at visible wavelength (see the schematic in **Figure 5**, ref. [48]).

© 2023 The Authors. Small Methods published by Wiley-VCH GmbH

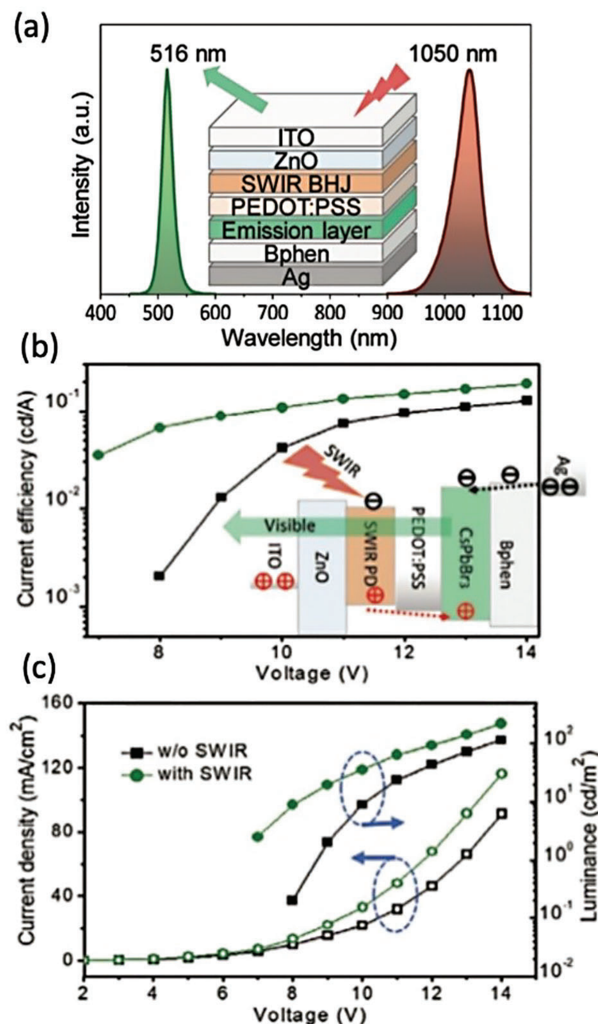

Figure 5. a) An example of integrated up-conversion structure comprised of an organic SWIR detector and a Perovskite LED emitting in the visible range (516 nm); b) corresponding band alignment and conversion efficiency; c) current density and luminance characteristics. Reproduced with permission under the terms of the Creative Commons CC BY license.[48] Copyright 2020, the Authors. Published by Wiley-VCH.

Notably, internal current amplification in the structure, such as that generated by using phototransistor detectors, enables improving the conversion efficiency.[49] The most promising reports on this kind of up-conversion devices are based on organic solution-processed materials such as OLED.[48,50] By integrating OLED with organic photodetectors (OPD), an up-conversion efficiency from near infrared light to visible of near 30% has been demonstrated,[51] while combining OLED with a phototransistor structure with internal gain has enabled an up-conversion efficiency of 1000%.[52] Electronic up-conversion-based CMOS infrared imaging can be implemented by scaling these architectures to the pixel level, provided that these device structures can be fabricated over large areas with good uniformity. In addition, particular care must be dedicated to limiting pixel cross talk, which might originate from both the parasitic lateral transport of photogenerated carriers and from the isotropic emission of the visible photons. One of the main advantages of up-conversion devices based on solution-processed and low-dimensional materials is that they can be readily deposited onto commercial CMOS imagers, eliminating the cost and complexity associated with crystalline growth of epitaxial structures to achieve up-conversion, and enabling low-cost and large-scale implementations.

2.2.3. In-Pixel Computation

Reducing the amount of data transmitted to the brain is a distinctive feature of biological vision, which enables its unparalleled energy and data efficiency.[53–56] Low-dimensional materials offer a unique platform for artificial synapses and neuromorphic computing, since novel electronic devices such as memtransistors [57,58] have been shown to replicate biological computation and learning in an energy-efficient manner.[59,60] These materials can be seamlessly integrated with low-dimensional photodetectors at the pixel level, mimicking biological vision to enable enhanced resolution at a reduced data transmission rate. Such architectures have been reported (see **Figure 6**) using for example MoS2 memtransistors for in-pixel early computation routines to achieve movement detection[61] and pattern recognition,[62] two distinct features of biological vision systems. Scaling these and other architectures based on low-dimensional materials and devices capable of in-pixel biological computation towards the megapixel count will require a full integration with conventional CMOS camera readouts to handle the amount of data and ensure information fidelity.

2.3. Polarization Sensitivity

Polarization-sensitive light detection (polarimetry), and especially passive imaging polarimetry enables to probe unique physical phenomena and objects which would be otherwise indistinguishable in conventional imaging techniques.[63–66] Low-dimensional materials enable unique polarization sensitivity thanks to their inherently anisotropic molecular structure or geometry, which results in asymmetric interaction with different polarization states of light. By taking advantage of their anisotropic properties, low-dimensional materials have been used to demonstrate both polarization-sensitive photodetectors as well as polarizing filters[47,67] as shown in **Figure 7**. Crucially, using some 2D materials for polarization filtering relies on accurate alignment of the polarization axis with the crystal orientation, and flakes including grain boundaries can result in inhomogeneous filtering. Conversely, low-dimensional materials that rely on their geometry for anisotropic light-matter interaction, such as nanowires can allow for fine lithographic control of the polarization filtering.

2.3.1. Ranging and Light Field Imaging

The intrinsically low optical absorption in atomically thin low-dimensional materials enables almost-transparent photodetectors which absorb only a small portion of the incident light. This in turn allows for full 3D light field imaging, where several

 © 2023 The Authors. Small Methods published by Wiley-VCH GmbH

23669608, 0, Downloaded from https://onlinelibrary.wiley.com/doi/10.1002/smtd.202300595 by Northwestern University Libraries, Wiley Online Library on [14/11/2023]. See the Terms and Conditions (https://onlinelibrary.wiley.com/terms-and-conditions) on Wiley Online Library for rules of use; OA articles are governed by the applicable Creative Commons License

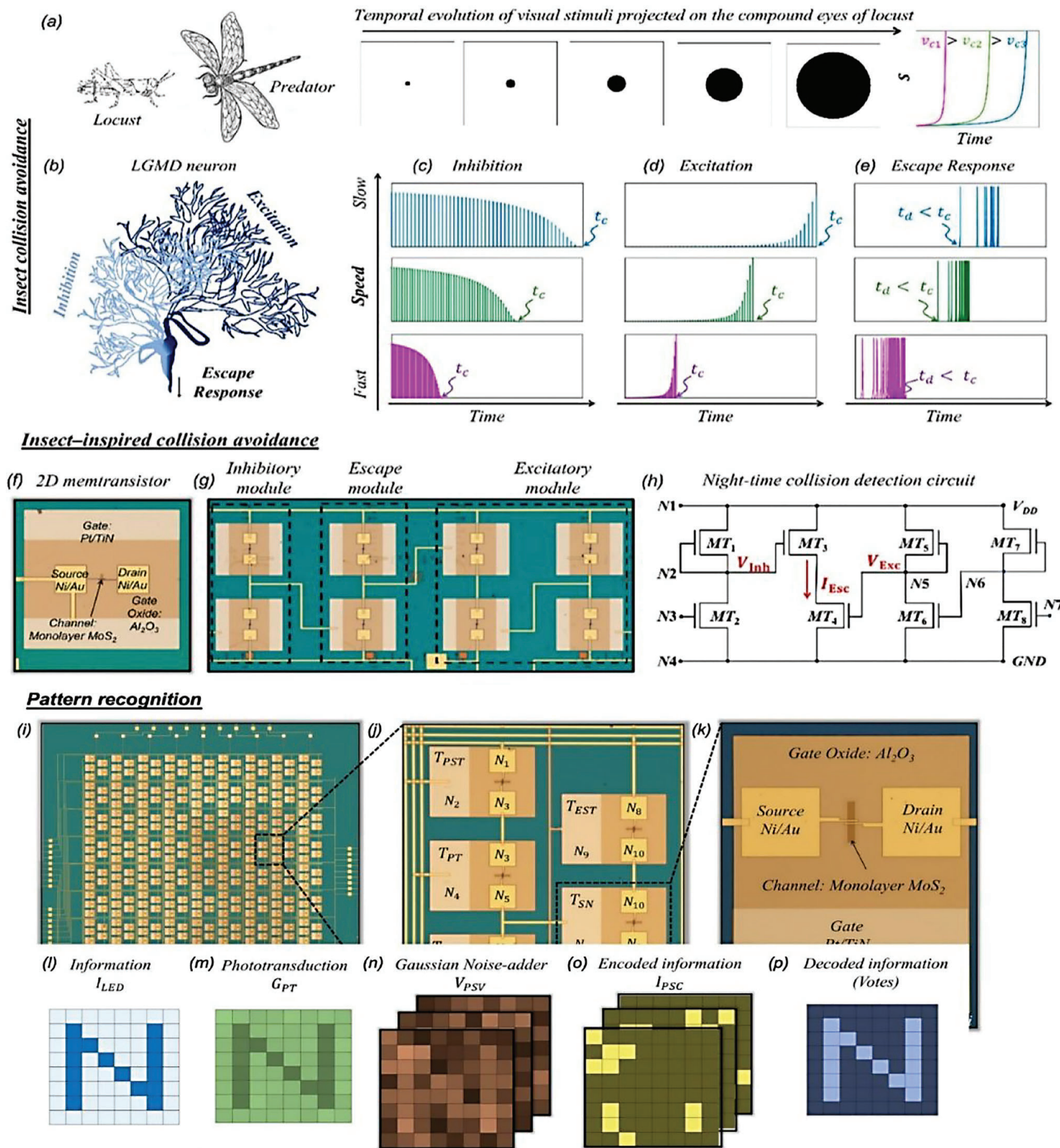

Figure 6. In-pixel computation using MoS_2 memtransistor array. a–h) Insect-inspired collision detection through in-sensor MoS_2 memtransistors. Schematic of a) collision-avoidance principle in insects and of b) the respective neural computation response. c) Time-resolved inhibitory, d) excitatory, and e) resulting escape e) responses tailored to the speed of an approaching object. f) Micrographs of a single memtransistor devices based on MoS_2. g) Micrograph and h) circuit schematic of the pixel-level neuromorphic computation module. Adapted with permission.[61] Copyright 2023, American Chemical Society. i–p) Imaging pattern recognition based on in-pixel MoS_2 memtransistor array. Micrographs of the i) imaging array, j) pixel module, and k) single memtransistor device. l–p) Shows the pattern recognition (p) of an original pattern information (l), encoded in gaussian noise (n,o). Reproduced with permission under the terms of the Creative Commons CC BY license.[62] Copyright 2022, the Authors. Published by Springer Nature.

© 2023 The Authors. Small Methods published by Wiley-VCH GmbH

23669608, 0, Downloaded from https://onlinelibrary.wiley.com/doi/10.1002/smtd.202300595 by Northwestern University Libraries, Wiley Online Library on [14/11/2023]. See the Terms and Conditions (https://onlinelibrary.wiley.com/terms-and-conditions) on Wiley Online Library for rules of use; OA articles are governed by the applicable Creative Commons License

23669608, 0, Downloaded from https://onlinelibrary.wiley.com/doi/10.1002/smtd.202300595 by Northwestern University Libraries, Wiley Online Library on [14/11/2023]. See the Terms and Conditions (https://onlinelibrary.wiley.com/terms-and-conditions) on Wiley Online Library for rules of use; OA articles are governed by the applicable Creative Commons License

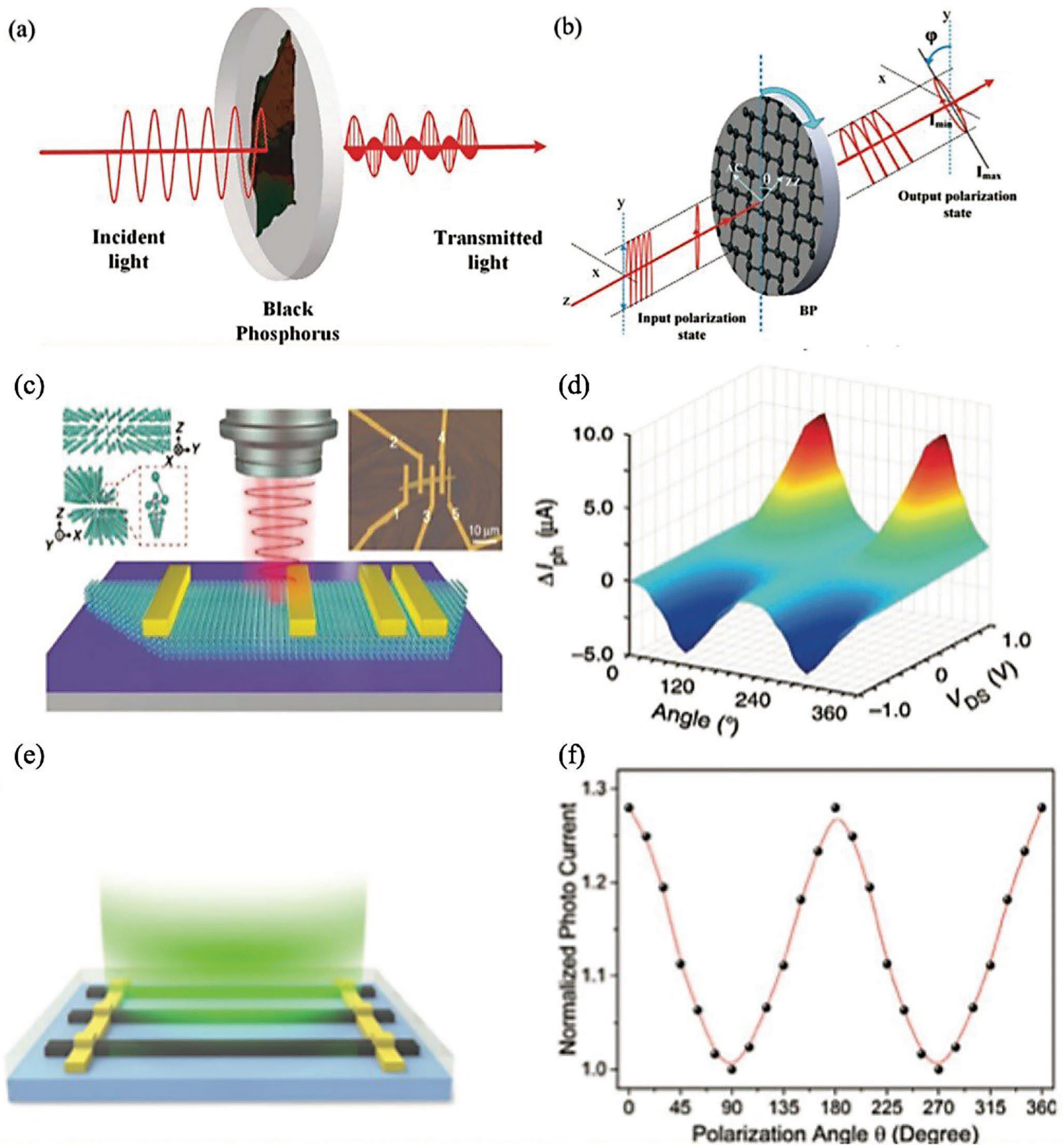

Figure 7. a,b) Black Phosphorus polarizing filter relying on the lattice orientation of the individual flakes for polarization selection. Adapted with permission.[68] Copyright 2017, American Chemical Society. Schematic of c) a polarization sensitive 2D photodetector based on monolayer Te, and d) relative photoresponse versus polarization angle. Reproduced with permission under the terms of the Creative Commons CC BY license.[31] Copyright 2020, the Authors. Published by Springer Nature. Schematic of e) a polarization sensitive 1D photodetector based on nanowires lithographically aligned to the polarization axis, and f) relative photoresponse versus polarization angle. Adapted with permission.[69] Copyright 2016, American Chemical Society.

© 2023 The Authors. Small Methods published by Wiley-VCH GmbH

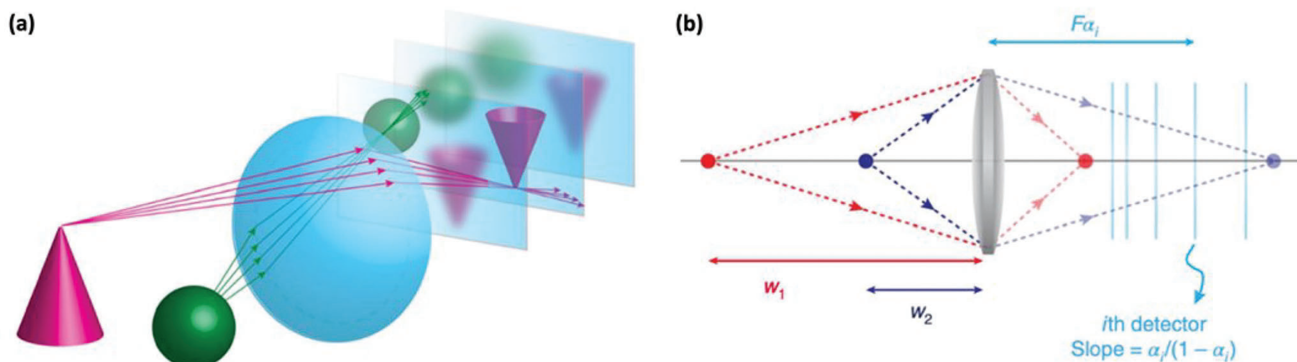

Figure 8. Concept of light field imaging using semi-transparent graphene photodetectors. a) Semi-transparent detector arrays can be placed along subsequent imaging planes without excessive light absorption hindering the image SNR. b) 3D object mapping can be achieved by leveraging the information obtained from multiple semi-transparent detector arrays along different imaging planes. Reproduced with permission.[20] Copyright 2020, Springer Nature.

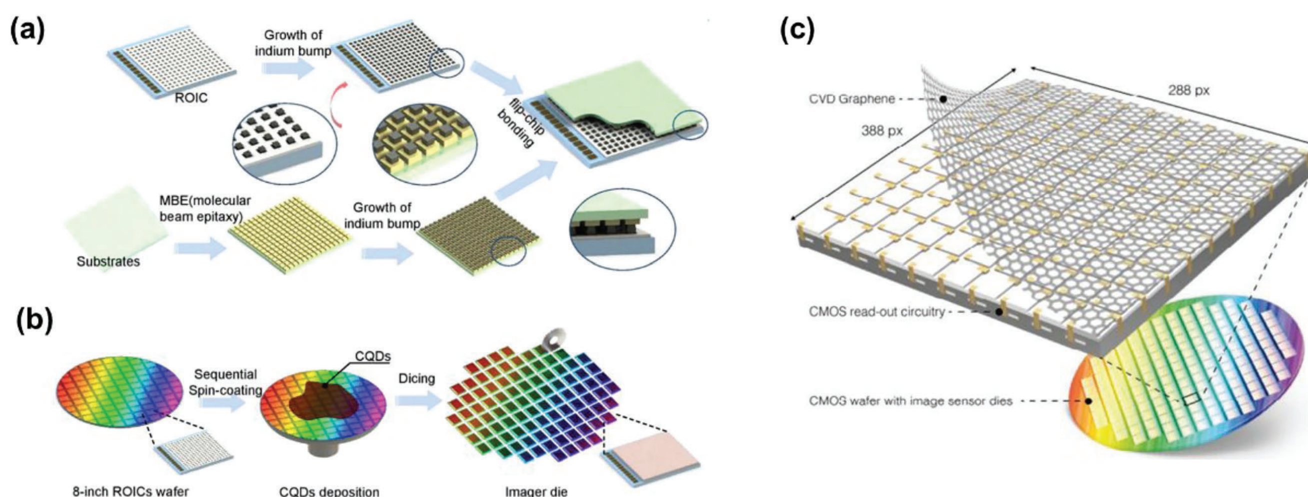

Figure 9. Fabrication process of a) conventional, and (b) CQDs-based infrared imagers. Adapted with permission.[70] Copyright 2023, American Chemical Society. c) A concept image of a 2D material-based infrared imager. Reproduced with permission.[30] Copyright 2017, Springer Nature.

detector arrays are placed at different focal planes of the imaging optics, to reconstruct the scene in 3D. Light field imaging has been demonstrated using stacked semi-transparent single-pixel graphene photodetectors.[20] Despite this bio-inspired single-pixel proof-of-concept demonstration, the full potential of this technique will require stacked full-frame focal plane arrays, as shown in **Figure 8**. This implementation remains quite elusive, and it will likely involve accessing the arrays of transparent detectors with semi-transparent read-out circuitry, or other alternative implementation to make each of the stacked imagers semi-transparent.

3. Integration of Low-Dimensional Material and Related Optics on CMOS Chips

The dominant infrared image sensors employ binary and ternary bulk semiconductors like InGaAs, InSb, and HgCdTe, which require expensive epitaxial growth processes to lattice-match with their growth substrates. In addition, to electrically interconnect the photodetectors made of these materials with the ROICs, the complicated indium bump formation and flip-bonding processes are imposed.[70] Even worse, this flip-chip bonding process is done at a single die scale, not wafer-level, because the detector substrate should be diced smaller than the ROIC chip to enable the wire bonding process. All these process steps lead to high cost and low production yield. Currently, these mature technologies have already been established and there is little room for any further cost savings. Recently, colloidal quantum dots (CQD) and 2D material have offered an attractive alternative to the existing infrared-sensitive materials by reducing the material growth cost and easing the integration process with the readout circuit (see **Figure 9**).

3.1. Integration of 0D Colloidal Quantum Dots

In early studies of CQD-based devices, solar cells and light–emitting diodes near the visible spectrum were the main focus. Recently, research on CQDs has extended towards longer wavelengths. As materials suitable for detecting infrared light, increasing attention has been focused on PbS and HgTe. The

© 2023 The Authors. Small Methods published by Wiley-VCH GmbH

23669608, 0, Downloaded from https://onlinelibrary.wiley.com/doi/10.1002/smtd.202300595 by Northwestern University Libraries, Wiley Online Library on [14/11/2023]. See the Terms and Conditions (https://onlinelibrary.wiley.com/terms-and-conditions) on Wiley Online Library for rules of use; OA articles are governed by the applicable Creative Commons License

bandgap of PbS CQDs can be tuned by changing their size, covering visible and short-wavelength infrared spectral bands. On the other hand, the bandgap of HgTe CQD, can be tuned to cover longer wavelengths due to the gap-less nature of bulk HgTe. Following early developments on single pixel configurations, recent efforts have been dedicated to integrating CQDs on image sensors. As a result, several companies have commercialized QD-based cameras in recent years. CQDs integration methods are very powerful, enabling electrical connection to ROICs with complex surface geometries through a simple spin-coating or casting method. A production cost analysis showed that CQDs can be produced for \$10–\$60 per gram[71] which is a small fraction of the manufacturing cost of the existing IR image sensor. Despite their significant maturity, imagers based on CQD suffer from limited carrier mobility and lifetime in CQD films.[72] These limitations are expected to be less significant in 2D material.

3.2. Integration of 2D Material

Since its discovery in 2004, Graphene has become one of the most studied materials, and as a result, it was awarded as one of the topics of the 2010 Nobel Prize.[73] Thanks to graphene's many attractive properties such as high transparency, tensile strength, and mobility, significant efforts have been made to its integration into various applications.[74] However, its application in field-effect transistors and photodetectors is prevented by its semi-metal gap-less nature.[75,76] For these reasons, many researchers started looking for various 2D materials with non-zero energy band gaps, such as transition metal dichalcogenide (TMDs), BP, and hBN. To utilize 2D materials for making image sensors, it is necessary to interface these materials with a CMOS chip that includes the driving and reading electronic circuits (i.e., ROIC).

In the initial phase of 2D material research, mechanical exfoliation from a bulk crystal using adhesive tapes. While simple, the domain size and thickness of the 2D materials obtained by mechanical exfoliation were random and unpredictable. In addition, the flake area is typically small and the method not easily scalable. Such properties have limited the practical application of this approach. An alternative method is the direct growth of 2D material. Growing 2D material on ROICs would be a highly preferred method in terms of scalability. Also, this method could potentially be free from defects and contamination caused by a transfer process and does not require additional cleaning steps. However, it is significantly challenging to deposit 2D materials with high quality directly on CMOS chips due to the non-catalytic property of the target substrates.[77] Some groups have showed the possibility of direct growth of 2D materials with high-quality by using a metal catalyst as vapor or coating type.[78,79] Moreover, research on directly growing high quality graphene on a dielectric substrate without using a metal catalyst has also been reported.[80] As mentioned earlier, it may be possible to directly grow high-quality 2D materials on CMOS substrates, but the critical issue is that most 2D materials grow at high temperatures ranging up to 900°C, which inevitability damages the CMOS chip.[81] Recently, research on growing 2D materials at low temperatures has also been reported,[82,83] but low-temperature growth does not yet produce high quality material.

Due to these issues, we believe that the most promising methods for the integration of 2D material on ROIC are based on either transfer or spin-coating. In the following sections, we will review these methods and discuss process compatibility for the realization of high-resolution imagers based on 2D materials. We will also discuss the most important challenges in the integration of 2D material with the existing ROIC chips, and propose solutions.

3.2.1. Transfer of CVD Grown 2D Materials

Using CVD and various transfer methods, considerable advancements have been made in producing high-quality large-area 2D material for practical application. The transfer methods of TMDs have generally originated from graphene transfer methods. Unlike graphene, however, the substrate for CVD growth of TMDs is not limited to transition metals (e.g., Cu and Ni) and could include various substrates such as Si/SiO_2, sapphire, and mica.[84] Currently, Si/SiO_2 substrates are the most commonly used due to their cost effectiveness and possibility of integration with large-scale integrated circuits. To transfer CVD-grown TMDs to a target substrate, it is necessary to separate the TMD film from the growth substrate as the first step. There are various methods for separating and transferring TMDs depending on the type of substrates and supporting layers. Here, we focus on two major separation methods classified into wet and dry lift-off (see **Figure 10**). However, the TMD transfer method could be more diverse depending on the supporting layer.[85]

Wet lift-off: When a metal substrate is used for the TMD's growth, the TMDs are released by wet etching of the metal. This method is costly since the expensive metal substrate is consumed, rendering it impractical for industrial applications.[85] On the other hand, when Si/SiO_2 substrate is used, TMDs can be separated using an etchant, such as NaOH or KOH, for the removal of the SiO_2 layer.[89] Although the silicon substrate is not completely dissolved, the strong etchant can damage the substrate surface, making it difficult to reuse the substrate. Recently, in an effort not to use wet chemicals, water-soluble sacrificial layers such as NaCl and NaSx, were inserted between the Si/SiO_2 substrate and the TMD layers. The TMDs separation is then performed with DI water.[90] Another lift-off method based on water utilizes the hydrophilic properties of the substrate for growth and the hydrophobic properties of the PDMS support substrate.[87] In this approach, PDMS is deposited on TMD on Si/SiO_2 substrates and then the wafer is exposed to water that penetrates only through the hydrophilic Si/SiO_2 interface, enabling the peeling of the hydrophobic TMD from the Si/SiO_2 substrate.

Dry lift-off: Using PDMS stamps, instead of water or chemical solution, methods from Si/SiO_2 substrate have been developed.[88] These methods are based on the difference in surface bond energy between PDMS and Si/SiO_2 substrate. The 2D material is separated from the growth substrate and transferred to the target substrate. However, since the surface energy of PDMS (19–21 mJ m^{-2}) is lower than that of Si/SiO_2 substrate (57 mJ m^{-2}), it is difficult to detach the 2D material from the substrate using PDMS. Therefore, a process to modify the surface energy of PDMS is required. The surface energy of PDMS can be modified higher than that of Si/SiO_2 substrate by vaporizing hydrophilic dimethyl sulfoxide (DMSO) on PDMS. As a result, when PDMS is attached to the TMDs on Si/SiO_2 and then

© 2023 The Authors. Small Methods published by Wiley-VCH GmbH

23669608, 0, Downloaded from https://onlinelibrary.wiley.com/doi/10.1002/smtd.202300595 by Northwestern University Libraries, Wiley Online Library on [14/11/2023]. See the Terms and Conditions (https://onlinelibrary.wiley.com/terms-and-conditions) on Wiley Online Library for rules of use; OA articles are governed by the applicable Creative Commons License

(a) Wet lift-off / Wet transfer

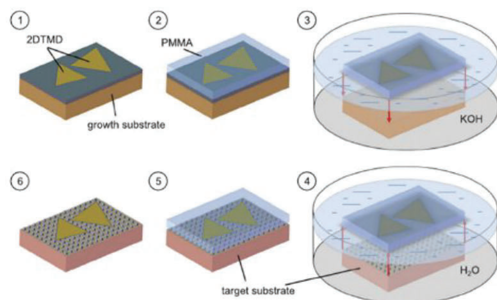

(c) Dry lift-off / Dry transfer

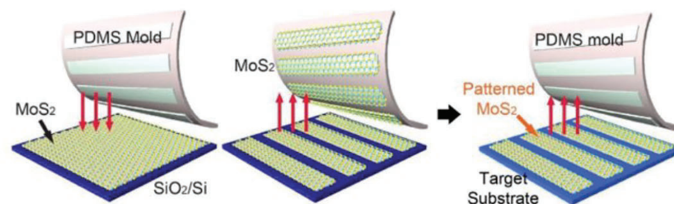

(b) Wet lift-off / Dry transfer

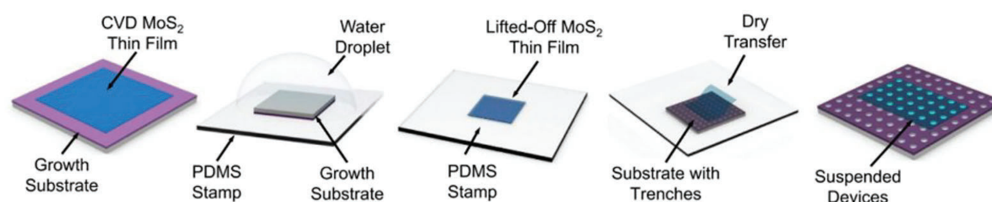

Figure 10. Concept Images showing different lift-off and transfer methods. a) Wet lift-off/wet transfer. Reproduced with permission under the terms of the Creative Commons CC BY license.[86] Copyright 2020, the Authors. Published by Taylor and Francis. b) Wet lift-off/dry transfer. Adapted with permission.[87] Copyright 2009, Royal Society of Chemistry. c) Dry lift-off/dry transfer of TMDs. Reproduced with permission.[88] Copyright 2017, Elsevier.

Table 3. Transfer method classification based on the support layer.

Support layer	Material	Transfer Classification	Reference
Polymer	PMMA	Wet (Solvent)	[60]
Polymer	PDMS	Dry (Surface energy)	[87–88,91–92]
Polymer	PPC	Dry (Surface energy)	[65]
Polymer	PS	Dry (Baking dissolution) Wet (Solvent)	[93,94]
Polymer	CA	Wet (Solvent)	[91]
Polymer	PC	Wet (Solvent)	[95]
Metal	Cu	Wet (Acid)	[96]

peeled off, the TMDs are transferred from the growth substrate to the PDMS. It is then necessary to reverse this effect and reduce the surface energy for the 2D material to separate them from the PDMS: when the PDMS/MoS_2 is brought into contact with the target substrate that is heated to 70 °C, the standard adhesion force of PDMS is restored and MoS_2 is released from PDMS to the target substrate.

Wet transfer and dry transfer: Similar to the classification of detachment method, the transfer method can also be divided into wet transfer and dry transfer categories (see Figure 10). This classification is mainly determined by the material of the supporting layer. For example, since PMMA is easily removed by solvents such as acetone, the related transfer methods are mainly wet transfer. On the other hand, PDMS material is classified as a dry transfer method because it is used to transfer 2D materials by stamping. **Table 3** classifies wet/dry transfer methods according to various supporting layer materials. For some methods, however, a combination of dry method and wet method may be used. This is because the transfer process requires not only the process of transferring the 2D material to the target substrate along with the supporting but also the process of removing the supporting layer at the end.

3.2.2. Spin-Coating of 2D Material

In terms of scalability, the CVD method adopted in other 2D materials should be very attractive. However, unlike other 2D materials, CVD growth for some low-dimensional materials, such as BP, are still lacking mainly due to their chemically active surfaces and the absence of suitable growth substrates.[97] For these materials, liquid-phase exfoliation is considered one of the most promising alternatives. Indeed, this approach is quite compatible with the integration of low-dimensional material to ROIC, and the process is quite scalable. Let us review this approach for BP. First, a chunk of black phosphorous crystal is immersed in solvents such as NMP,[98] CHP,[99] DMF, and DMSO.[100] Then sonication is used to break down the interlayer vdWs. While details of the process could be slightly different, depending on the material and the solvents used, it involves repeated removal of larger solid parts using centrifuge separation methods. The final purified solution is spin-coated or drop-casted on the target substrate. Interestingly, the liquid phase exfoliated BP nanoflakes show competitive properties compared to mechanically exfoliated flakes.[100] In addition, material degradation in this approach seems to occur less than

 © 2023 The Authors. Small Methods published by Wiley-VCH GmbH

23669608, 0, Downloaded from https://onlinelibrary.wiley.com/doi/10.1002/smtd.202300595 by Northwestern University Libraries, Wiley Online Library on [14/11/2023]. See the Terms and Conditions (https://onlinelibrary.wiley.com/terms-and-conditions) on Wiley Online Library for rules of use; OA articles are governed by the applicable Creative Commons License

mechanical exfoliation potentially due to the protective effect of the solvent shell against nanosheets' reaction with oxygen and water.[99] The low-temperature nature of this approach, the compatibility of the solvents to ROIC material, and the scalability of spin-coating to wafer-scale production are significant advantages of this approach. However, this method negates some of the most important aspects of low-dimensional material since the end material is a random ensemble of particles. Overall, we believe this method has a lot of merits and could be readily adopted for the realization of high-resolution imaging chips in challenging spectral bands, such as mid-wave infrared, deep UV, THz, and X-ray.

3.2.3. Challenges in Integration on the Existing ROIC Chips

To produce uniform images, the electrical and optical properties of the integrated 2D material should be very uniform across the entire wafer area—generally within a few percent. To do so, not only the techniques that produce and integrate the 2D material must be uniform, but also the surface condition of the ROIC wafer should be considered. Since the existing ROICs are designed for the flip-chip bonding process, as discussed in the Introduction, they include tiny indents where the indium bumps are to be formed. This feature improves the alignment of the indium bumps on the bond electrodes during a "reflow" step. However, these indents are not suitable for transferring 2D materials on ROICs as they reduce the probability and quality of van der Waals bonds between the 2D material and the ROIC electrodes.

The next major challenge also originated from the special design of the current ROICs. A CMOS wafer consists of a large number of ROIC chips, each surrounded by an array of wire-bonding pads. While integrating the 2D material, the wire-bonded pads must be protected from the 2D material deposition. While conventional photolithography, etching processes, or taping could be used to achieve this, we have observed that performing these additional steps after transferring 2D material could lead to the degradation of yield and performance of the transferred 2D material. These issues are even more significant for integration at a chip level (i.e., on diced ROIC chips) due to the proximity of the wire-bonding pads to the edges of the chip and the resulting photoresist edge beads formation.

While many processing tricks could be used to achieve working imagers, our recommendation is to redesign ROIC chips with the following minimal changes for integration with low-dimensional materials:

1) The surface of the imaging array must be flat, with pixel electrodes slightly protruding from a matrix of dielectrics (e.g., tungsten plugs surrounded by the top oxide or nitride layers).
2) Top wire-bonding pads must be recessed by a few microns from the top surface and the top metal must be gold and not the typical aluminum.
3) Backside bond pads are ideal replacements for wire-bonding pads. While these cannot be easily used in conventional ROIC due to the indium bump-bonding, 2D material integration does not need bump-bonding and can significantly benefit from backside bond pads.

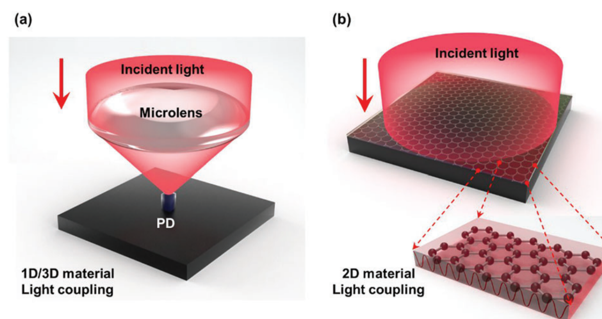

Figure 11. The concepts of a) far-field concentrators and b) near-field concentrators.

3.3. Integrated of Far-Field and Near-Field Light Concentrators

Most 2D materials have limited light absorption due to their small thickness. One monolayer of graphene only absorbs ≈2.3% of normally incident light even though it has remarkably high absorption for an atomically thin layer.[101] Recent studies suggest that other 2D materials have a similar level of absorption.[102] As we pointed out earlier, a small optical absorption probability leads to a small quantum efficiency of light detection. While the total optical absorption of low-dimensional material can be increased by stacking or aggregating them, these approaches negate many of the benefits resulted from their extremely small size in one or more dimensions. In contrast, solutions that concentrate electromagnetic waves onto the low-dimensional material can increase their quantum efficiency while maintaining other benefits, such as enhanced sensitivity due to their low capacitance. In the following, we review these solutions categorized as far-field and near-field concentrators (see **Figure 11**).

3.3.1. Far-Field Concentrators

Advanced CMOS image sensors with small pixel sizes face a similar issue since the photosensitive area of a pixel constitutes a fraction of the total pixel area, which is called the pixel fill-factor. These image sensors utilize a microlens array to increase their fill-factor. Each microlens in the array focuses the light incident on a pixel to the photosensitive area as shown in Figure 11a. However, this method cannot be used for imagers operating outside the silicon absorption range due to its incompatibility with the bump-bonding fabrication method. Recently, several groups have demonstrated new approaches in the integration of microlenses as an "immersion lens array" with such imaging sensors.[103,104] These methods are compatible with the realization of low-dimensional image sensors when the deposition of suitable dielectric layers on the low-dimensional material is possible.

These approaches employ back-illuminated structures, where photons travel across a dielectric layer. Therefore, they have a moderate numerical aperture due to the relatively long focal lengths ranging from several tens to hundreds of microns. Meanwhile, most imagers based on low-dimensional material cannot include a very thick dielectric deposition, so it is difficult to design far-field optics with a reasonable numerical aperture. Even if microlenses can be combined with low-dimensional material,

 © 2023 The Authors. Small Methods published by Wiley-VCH GmbH

23669608, 0, Downloaded from https://onlinelibrary.wiley.com/doi/10.1002/smtd.202300595 by Northwestern University Libraries, Wiley Online Library on [14/11/2023]. See the Terms and Conditions (https://onlinelibrary.wiley.com/terms-and-conditions) on Wiley Online Library for rules of use; OA articles are governed by the applicable Creative Commons License

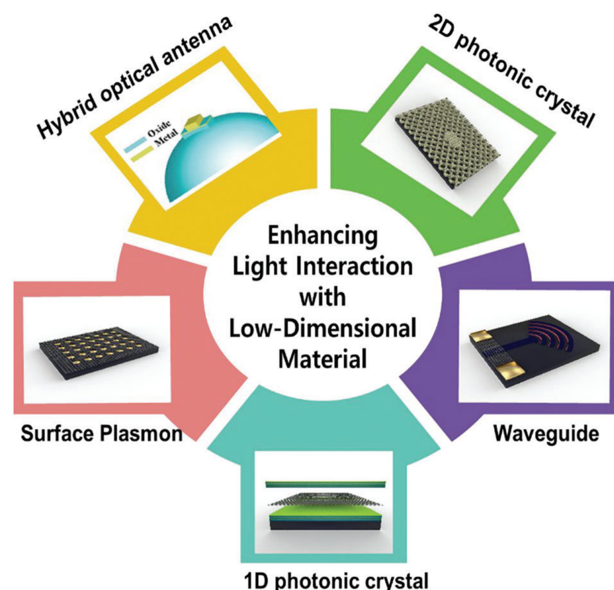

Figure 12. A summary of different methods to enhance light-matter interaction in low-dimensional material: a) Surface plasmon polaritons device structures using metallic nanostructures, b) waveguide, c) 1D photonics, d) 2D photonic crystal structure, and e) broadband and low-loss metallo-dielectric hybrid structures.

two issues remain challenging: the focused beam may not be fully absorbed by an ultra-thin 2D material, and the alignment of the focal point and a small absorber is challenging due to the large vertical distance between the two. That is, the traditional lens method of converging light into a single point on a plane seems to be insufficient for low-dimensional material.

3.3.2. Near-Field Concentrators

An alternative method is to couple a normal-incident light to a surface mode near the 2D material plane. A summary of different near-field concentrators is shown in **Figure 12**.

One of the most powerful methods is to integrate metallic nanostructure with 2D material for creating surface plasmon polaritons (SSP), which is a collectively coherent electron oscillation as the formation of dipoles in the metal due to electromagnetic waves of incident light.[105] The plasmonic effect is strongly dependent on the material composition, size, shape, and periodicity, so various structures have been explored.[106,107] The SSP generates a strongly enhanced optical field in the local region between a metal and a dielectric, giving rise to strong light-matter interactions in the specific hot spot locations. However, a drawback of plasmonic nanostructures is that they suffer from large ohmic losses by metal absorption.[108,109] The metal loss is less significant at longer wavelengths and hence this approach is most suitable for mid- and long-wavelength infrared bands. In addition, plasmonic structures require sub-wavelength patterns that are less stringent at longer wavelengths and can be made with conventional photolithography. While the nanoscale features required for SSP at shorter wavelengths were originally deemed a major challenge for industrial adoption, high throughput nanopatterning methods such as nano-imprint lithography[110] and microsphere projection lithography[111,112] are promising solutions.

Another method capable of boosting light-matter interaction in low-dimensional material is based on waveguides.[113,114] Waveguide structures consist of a core layer with a higher refractive index and a cladding layer with a lower refractive index. They can enhance light-matter interaction by coupling the normal-incident light to the waveguide optical modes. Waveguide structures using spin-coating of polymer material serving as cladding layers both on and underneath the stripe-patterned graphene have been proposed.[115] Similarly, Si or SiN layers have been used to achieve high-speed low-dimensional photodetectors.[116] However, waveguide methods have several problems when applied to an image sensor. First, the mechanisms used for coupling light to the waveguide are usually narrowband. Therefore, these structures lead to imagers with narrow spectral sensitivity. Second, most waveguide structures impose a large footprint that is difficult to implement within the small pixel area of image sensors.

Combining 2D photodetectors with one- and two-dimensional photonic crystal presents another approach for increased light absorption.[117,118] For example, a 1D photonic crystal structure was designed to have two Bragg mirrors surrounding a graphene layer by depositing alternating layers of a high-dielectric constant material and a low-dielectric constant material. In this structure, incident light is reflected back and forth due to the two Bragg mirrors trapping the light and thus enhancing the light absorption.

Similarly, 2D photonic crystal structures have been realized by forming periodic nano-hole or nano-rod patterns via dry etching of dielectrics, such as Si or SiO_2, forming a periodic refractive index. Such a structure produces a photonic bandgap that prevents light propagation at a specific wavelength band and effectively traps the light within the intended area.[119,120] While more efficient in concentrating the light intensity, it has the same issue of a narrow operating wavelength band and a narrow light incident acceptance angle. As a result, waveguide or microcavity structures may be suitable for applications with specific operating wavelengths and angles, such as spectroscopy, but are not suitable for a broad range of applications that require sensitivity to broadband electromagnetic waves with wide incidence angles.

An alternative approach that is relatively broadband is based on hybrid optical antenna that combines metallic and dielectric structures to achieve a high optical concentration across a broad spectral band.[121] The broadband dielectric antenna that is based on the so-called Photonic Jets can be only a few wavelengths wide. It couples the EM field from free-space to a sub-wavelength metallic cavity around the photosensitive region of the device. The combination of the metallic cavity and the absorber produces a very short photon lifetime, which means a wide spectral absorption due to the uncertainty principle.

4. Photodetector Characterization Based on ROIC

Testing low-dimensional photodetectors requires special care since these devices have low signal levels and require low noise measurements. In fact, lack of proper measurement has led to a rather widespread inaccurate reported results from such photodetectors.[122] There are extensive reports and reviews about the theoretical treatment of noise in solid-state

© 2023 The Authors. Small Methods published by Wiley-VCH GmbH

23669608, 0, Downloaded from https://onlinelibrary.wiley.com/doi/10.1002/smtd.202300595 by Northwestern University Libraries, Wiley Online Library on [14/11/2023]. See the Terms and Conditions (https://onlinelibrary.wiley.com/terms-and-conditions) on Wiley Online Library for rules of use; OA articles are governed by the applicable Creative Commons License

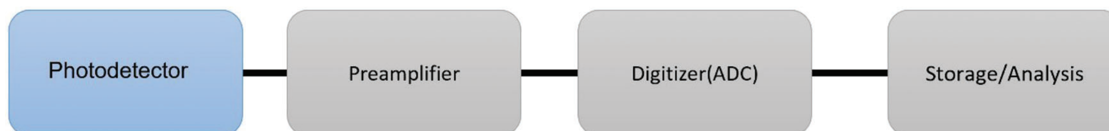

Figure 13. Schematic of general components of a measurement setup.

devices and photodetectors,[123,124] the definition of figures of merit, and the general limitations and proper characterization of photodetectors[125–129] in the literature. Therefore, we wish to focus our review on a less explored and quite powerful method of characterization of such devices using ROIC chips and electronics. We show the unique advantages of this approach to achieve extremely low measurement noise and other unparalleled properties.

Generally, a proper measurement setup should be able to produce sufficient information about the photodetector under tested to extract key parameters such as detectivity, noise-equivalent power, and bandwidth. To meet this end, the measurement setup should have noise levels that are low enough to provide a good signal to noise ratio (SNR) in data collection and the measurement sampling rate (speed) needs to be high enough that the collected data accurately reflects the device performance. Accurate noise measurement in low-dimensional devices is one of the most challenging characterization steps.

Generally, the most important building blocks of a measurement setup are a preamplifier and analog to digital converter. The schematic of a measurement setup is shown in **Figure 13**. Preamplifiers can amplify the device's voltage, current, or charge. Charge amplifiers use capacitive feedback to integrate the input current into an output voltage that is proportional to the charge, which in turn is proportional to the total number of incident photons. Therefore, use of charge amplifiers is typically preferred for imaging arrays since the pixel signal needs to be proportional to number of incident photon per pixel during an integration time. Signals collected from the measurement setup are usually converted to digital data, using analog-to-digital converters, and stored for further processes or analysis. The most common method for testing photodetectors is based on probing and wire bonding. Metallic probes are used to make electrical contacts to devices and benchtop tools are used to collect data. As we shall see, however, this approach has significant issues when used for measuring very low levels of noise. To address some of these issues, a combination of fan-out and wire bonding has also been used. However, this method is still not sufficient for measuring devices with very low noise levels.

This section is divided into two main parts. In part one, we compare the noise level of ROICs and probe stations and establish that ROICs can provide a significantly higher SNR. In part two, we discuss the benefits of using cameras as test beds for parallel evaluation of thousands of devices.

4.1. Limits of Noise Measurement

We evaluate the minimum noise limit of a measurement system by analyzing its two major components of noise: the internal electronic noise, and the external interference noise.

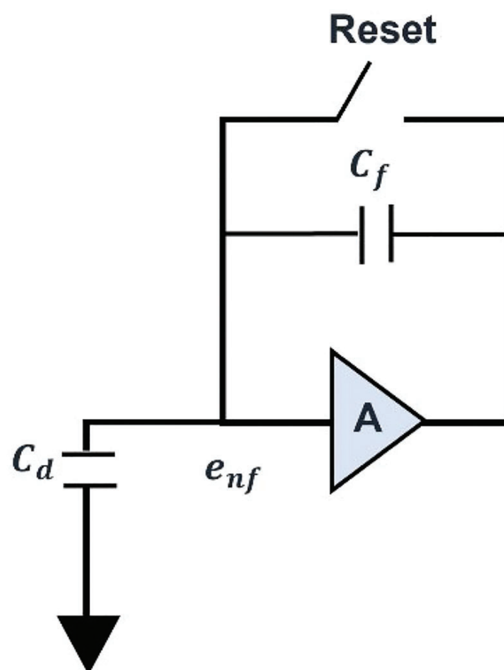

Figure 14. The simplified circuit of a charge amplifier connected to a photodetector.

4.1.1. Electronic Noise

For studying the noise in a measurement setup, analyzing the first stages (charge collection and amplification) is typically sufficient since the total noise is mostly dominated by the first stage, according to the Friis formula.[130] To evaluate the first stage of a measurement setup, a photodetector with extremely low dark current can be modeled as a capacitance C_d. The charge amplifier is simplified as an integrator circuit with a feedback capacitance C_f and a reset button that dumps the charge at the end of each measurement interval. The signal-to-noise ratio expression for this circuit, shown in **Figure 14**, can be evaluated as[131]

$$\frac{Q_s}{Q_n} = \frac{Q_s}{A\sqrt{\Delta f_n} e_{nf}\left(C_d + C_f\right)} \tag{1}$$

where Δfn and A are the noise bandwidth and the gain of the amplifier, respectively. As Equation (1) shows, the total capacitance of the system governs the noise in this system. Any method used to connect the amplifier to the detector will add parasitic capacitance to the denominator of the Equation (1), further decreasing the SNR. The effect of this parasitic capacitance is significant when the device has a very small capacitance, as is the case for many low-dimensional devices. Here, we perform

© 2023 The Authors. Small Methods published by Wiley-VCH GmbH
23669608, 0, Downloaded from https://onlinelibrary.wiley.com/doi/10.1002/smtd.202300595 by Northwestern University Libraries, Wiley Online Library on [14/11/2023]. See the Terms and Conditions (https://onlinelibrary.wiley.com/terms-and-conditions) on Wiley Online Library for rules of use; OA articles are governed by the applicable Creative Commons License

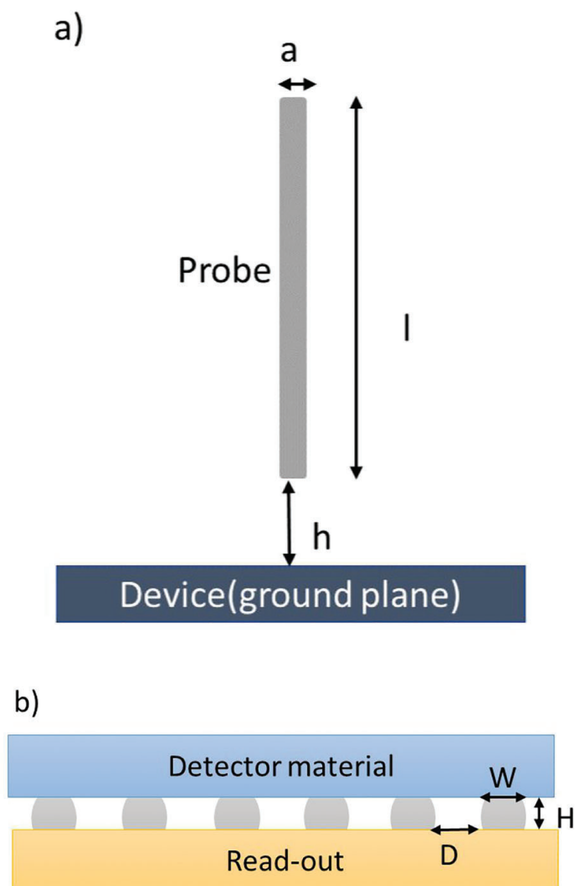

Figure 15. a) Shows a conductor perpendicular to the ground plane. b) Shows the bump bonding to ROIC.

an order-of-magnitude comparison of this parasitic capacitance for the commonly used probing measurement and the proposed ROIC measurement method.

A probe landed on a device can have multiple parasitic capacitances to different objects in its vicinity. Assuming the best case scenario (i.e., minimum capacitance), the probe can be seen as a conductor perpendicular to the ground. The capacitance of this simplified system can be estimated as[132]

$$C = \frac{2\pi\epsilon l}{\ln\left(\frac{l}{a}\right) - 2.303 D_2} \tag{2}$$

In this equation, ϵ is the permittivity of the dielectric material, l is the length of the wire, and a is the wire diameter (**Figure 15**a). D_2 is a parameter dependent on the ratio of the distance between the conductor and the ground h and the length of the conductor. Equation (2) suggests that the increase in the probe length will increase the capacitance. Some estimated values of capacitance for metallic probes are shown in **Table 4**. To calculate these estimations, we used the ratio of device heights to typical probe lengths to find D_2. The values for D_2 in the table were found by extrapolating the values given in ref. [132]. The permittivity in this calculation is the permittivity of vacuum for the sake of simplicity. When the substrate permittivity is considered, the capacitance values of **Table 5** will be bigger.

Table 4. Some estimated capacitance values for probes.

l (mm)	a (μm)	h/l	D_2	C (fF)
15	50	2e-4	0.422	176.33
15	5	2e-4	0.422	118.62
5	50	6e-4	0.421	76.52
5	5	6e-4	0.421	46.85

Table 5. Estimated capacitance values of ROIC indium bumps.

Pixel pitch (μm)	Width (μm)	Height (μm)	C (fF)
10	5	10	0.044
30	10	10	0.0295

To model the parasitic capacitance of a ROIC, capacitance of bump bonds is considered. Micro bonds are studied in ASIC design for the delay and power dissipation they cause. Similar approximations are used in this study to model the capacitance of the ROICs' bump bonds. A simple equation for the capacitance can be written as[145]

$$C = \frac{\epsilon H W}{D} \tag{3}$$

where D is the pixel pitch, ϵ is the permittivity of the dielectric material, and H and W are the bump height and width, respectively (Figure 15b). The capacitance of the nearest neighbors is the biggest term and is used in the estimations of Table 5. For these estimates the permittivity is again assumed to be vacuum permittivity. These values serve as a comparison of order of magnitude, rather than the exact capacitances.

A comparison of values in Tables 4 and 5 shows that the capacitance in the ROICs can be significantly smaller than probes. Based on Equation (1), the noise level achieved with a ROIC cannot be achieved with a probe. Such a low parasitic capacitance values combined with the fact that commercial ROICs with less than 10 electron-rms noise per measurement exist today,[146,147] allow photodetector noise measurement well below Femto-Ampere $\text{Hz}^{-0.5}$.

4.1.2. Interference Noise

A typical test environment is flooded with electromagnetic waves of different origins and frequencies. The electromagnetic interference (EMI) effect is seen as an extra component of noise in measurement systems and can be very significant for small signal levels. Manmade sources of EMI are only growing in number and power. **Table 6** shows some of the most common manmade EMI sources at different frequencies.

Since most of such sources cannot be controlled, EMI shielding mechanisms are very important in reducing the measurement system noise. Mechanisms of shielding can be categorized as reflection, absorption, and multiple reflection (from different interfaces of the shield).[148] A simplified model for the penetration (skin) depth of EMI helps with our understanding

© 2023 The Authors. Small Methods published by Wiley-VCH GmbH

23669608, 0, Downloaded from https://onlinelibrary.wiley.com/doi/10.1002/smtd.202300595 by Northwestern University Libraries, Wiley Online Library on [14/11/2023]. See the Terms and Conditions (https://onlinelibrary.wiley.com/terms-and-conditions) on Wiley Online Library for rules of use; OA articles are governed by the applicable Creative Commons License

Table 6. Typical manmade sources of EMI.

Source	Frequency
AC line	60 Hz
Monitors, fluorescent lights	120 Hz
AM radio	30 kHz–3 MHz
Aviation communication	3–30 MHz
FM radio	30–300 MHz
Wireless communication and GPS	300 MHz–3 GHz
5G, satellites, WiFi	3–30 GHz

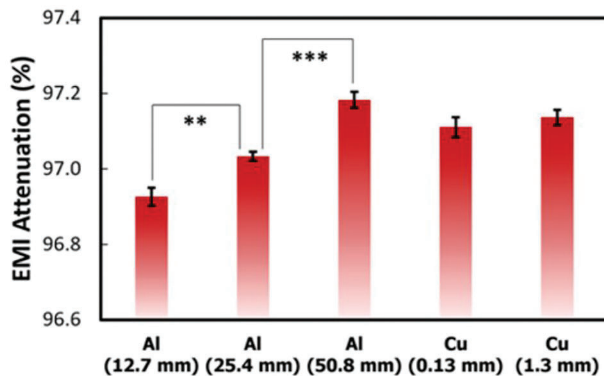

Figure 16. The highest attenuation achieved requires about 50.8 mm-thick Aluminum. Reproduced with permission.[149] Copyright 2022, American Chemical Society.

of the relation between shielding material thickness and reflection/absorption. The skin depth formula presents the thickness within which EMI can effectively penetrate:

$$\gamma = \frac{1}{\sqrt{\pi \sigma f}} \tag{4}$$

$$E(z) = E_0 \, e^{-\frac{z}{\gamma}} \tag{5}$$

In these equations, E_0 is the electric field amplitude before entering the material, f is frequency, σ is conductivity, γ is the skin depth, and t is the shield thickness. Equation (4) shows the skin depth formula and Equation (5) shows the decay of the electric field in the shielding material at distance z. The equations suggest that at higher frequencies and higher conductivity thinner materials are needed to shield effectively. This simple model is valid for a single sheet of material as the calculations for a Faraday box are more complicated. Yet, the general relation between shielding thickness and frequency holds. Some popular shielding materials are metals like aluminum and copper that can reflect and absorb EM waves. The skin depths in best metals tend to be very large for lower frequencies. To have an effective shielding, the thickness of the material needs to be multiple times bigger than the skin depth. Glasscott et al. [149] have conducted a study of different Faraday cage designs and their EMI shielding strengths. **Figure 16** shows what thickness of material results in a certain percentage of attenuation. Even for a very thick 50.8 mm shield, the EMI attenuation reached only 98%. In short, it is very difficult to shield a measurement setup from EMI. Therefore, the best EMI noise immunity requires reducing the picked-up EMI power by reducing the effective antenna cross-section of the measurement setup.

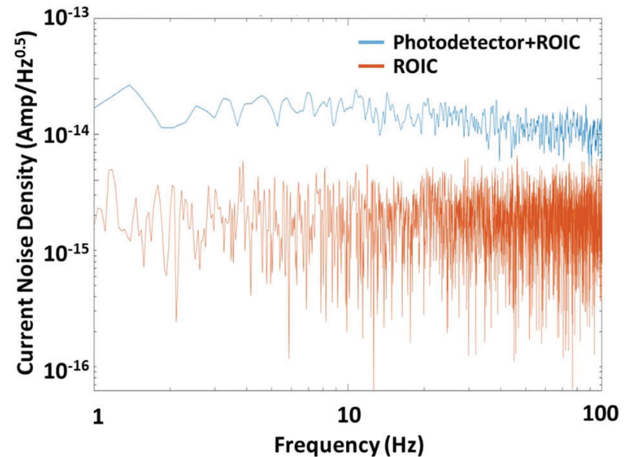

Figure 17. Noise analysis of a bonded phototransistor and a bare ROIC.

To compare the EMI noise picked up by a probe versus a ROIC, a simple short dipole antenna model is used here. Equation (6) shows the EMI induced voltage noise in a wire.[150,151]

$$V_n = E_0 \, d \sqrt{\frac{5\pi G}{\eta}} \tag{6}$$

where d is the length of the antenna (probe length in a setup), G is antenna gain (a constant value), η is the ambient impedance, and *E0* is the amplitude of the EMI field. As Equation (6) suggests, the significantly larger lengths of probing conductors in a probing test system result in much higher EMI noise. Since effective shielding for low noise applications can be hard, using a read out integrated circuit for measurement alleviates the pickup problem since the detectors are directly connected to preamplifier and the entire measurement system can be very compact (the distance become in orders of 10 s of microns instead of millimeters). Note that in this analysis, we have ignored the detrimental effects of the wires connecting the probe to the preamplifier, which could occasionally be much bigger than the probe itself.

4.1.3. Example of Photodetector Noise Measurement Using ROIC

Here we show an example of noise measurement using ROIC, where a chip with phototransistor nanowire detector array is bonded to a commercially available ROIC (FLIR, ISC9809). The test was performed at a ROIC mode with 700 electron-rms noise and the measurement was done at a temperature of 140K in dark conditions. Given the data collection time, the 700 electron-noise (rms) corresponds to about 2.3 Femto-Amperes Hz$^{-0.5}$. **Figure 17** shows the noise spectrum of one of the ≈80 000 photodetector pixels and the noise spectrum of the bare ROIC pixel (no photodetector is bonded to the ROIC). The EMI at 60 Hz and its harmonics can be seen here, though heavily suppressed to below a noise spectral density of ≈3 Femto-Amperes Hz$^{-0.5}$.

© 2023 The Authors. Small Methods published by Wiley-VCH GmbH

23669608, 0, Downloaded from https://onlinelibrary.wiley.com/doi/10.1002/smtd.202300595 by Northwestern University Libraries, Wiley Online Library on [14/11/2023]. See the Terms and Conditions (https://onlinelibrary.wiley.com/terms-and-conditions) on Wiley Online Library for rules of use; OA articles are governed by the applicable Creative Commons License

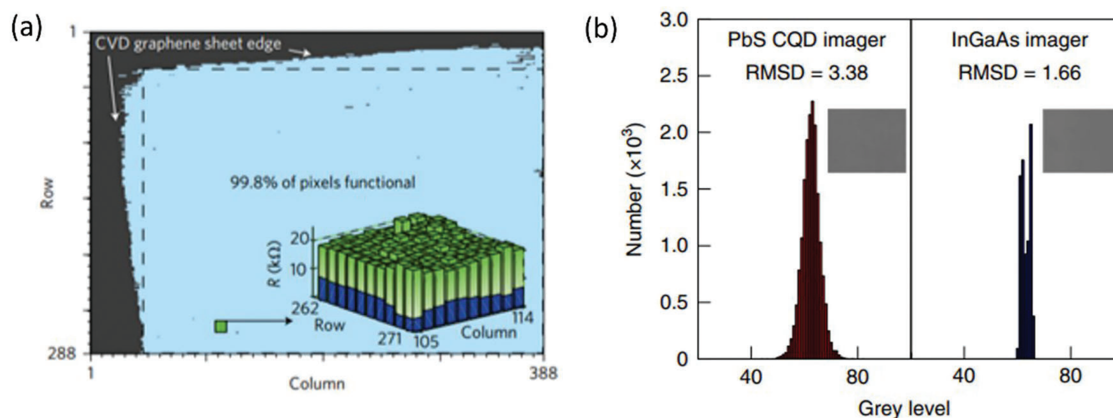

Figure 18. a) CVD-grown graphene integrated on a ROIC (blue area). The inset is a histogram of pixel resistance in the blue region, showing 99.8% of pixels are functional. Reproduced with permission.[30] Copyright 2017, Springer Nature. b) Statistical evaluation of the device uniformity for a PbS CQD detector array using a histogram plot of photoresponse of thousands of devices integrated on a ROIC. This method allowed an accurate comparison with a commercial InGaAs imager. Reproduced with permission.[152] Copyright 2022, Springer Nature.

4.2. Camera as a Testbed

As it was established in the previous section, the noise of the ROICs is far lower than conventional probes. However, having a low noise is not the only benefit that testing devices with ROIC can offer. Existing ROIC designs allow testing tens of thousands to millions of detectors in parallel. Also, existing electronics allow rapid collection of a large amount of data from the ROIC, all at near-identical measurement condition and setpoint (temperature, input power, bias voltage, etc.) Collecting such a massive amount of data from a large number of devices with near-identical condition enables unprecedented statistical analysis of devices.

In addition, the stability of this approach allows averaging the data collection for each device over a significant time, which leads to an increased SNR for ultra-low photon flux applications. Another important benefit is that the effect of variation in the device fabrication is minimized since all devices on a chip are processed simultaneously. As such, comparison of their figures of merit with respect to engineered features, such as device size, can be compared more accurately. This ability allows proper statistical evaluation of different devices in producing a mathematical measure of confidence in the reported data, which is a frequently overlooked issue in currently reported results from low-dimensional devices. In the following subsections, some of these merits in using ROIC for photodetector measurement are explored through examples of published research.

4.2.1. Statistical Analysis of Uniformity and Reproducibility

The statistical analysis of the large amounts of pixels produces a mathematically sound evaluation of the functionality of a novel photodetector. For example, integrated PbS CQD on CVD grown graphene photodetector integrated on a 388 × 288 ROIC shows photogating effect is the mechanism of the photoresponse in the array.[30] The quantum dots provide photogenerated carrier for the graphene layer and the change of conductivity in the graphene is captured by the ROIC. For the imager to work, the resistance range of the material must be compatible with the ROIC. The authors demonstrated the statistical average and standard deviation of the device resistance with high confidence (**Figure 18**a). They also produce a statistically meaningful value for the yield of the whole fabrication process, which is crucial information when this technology is to be used for any application.

Similarly, a recent study[152] based on PbS CQD photodiodes on a CMOS ROIC with 640 × 512 pixels provides statistical data on the fabrication uniformity and device reproducibility. A grayscale chart is imaged by the PbS CQD imager and compared with a commercial Hamamatsu InGaAs imager. The histogram of grayscale response of each of the imagers was used to compare the pixel uniformity in a mathematically accurate method, as shown in Figure 18b.

4.2.2. ROIC for High-Throughput Experiments

In addition to statistical analysis, simultaneous measurement of a large number of devices allows for a systematic study of the physics involved and the parameters affecting the performance of photodetectors. As the size of devices shrink, the impact of inherent nonuniformities of different nano-fabrication steps on the device performance becomes more significant. Such nonuniformities introduce a substantial randomness in the measurement results, rendering comparison of a small population of devices inaccurate. This issue is quite significant in low-dimensional devices. As such, comparing a few devices does not produce a statistically sound evaluation. Our group has developed a ROIC-based high-throughput testbed approach to study low-dimensional photodetectors. For example, to explore the effect of device size on the sensitivity of phototransistors, our group has integrated an array of 1 and 2 μm diameter devices to a conventional ROIC.[15] Earlier, we developed a theoretical model that suggested the sensitivity limit of low-dimensional devices must primarily depend on their junction capacitance[13,14] and wanted to confirm this model with a high confidence experimentally. Simultaneous fabrication of devices with two different diameters (1 and 2 μm) on a single ROIC allowed precise evaluation of our

 © 2023 The Authors. Small Methods published by Wiley-VCH GmbH

23669608, 0, Downloaded from https://onlinelibrary.wiley.com/doi/10.1002/smtd.202300595 by Northwestern University Libraries, Wiley Online Library on [14/11/2023]. See the Terms and Conditions (https://onlinelibrary.wiley.com/terms-and-conditions) on Wiley Online Library for rules of use; OA articles are governed by the applicable Creative Commons License

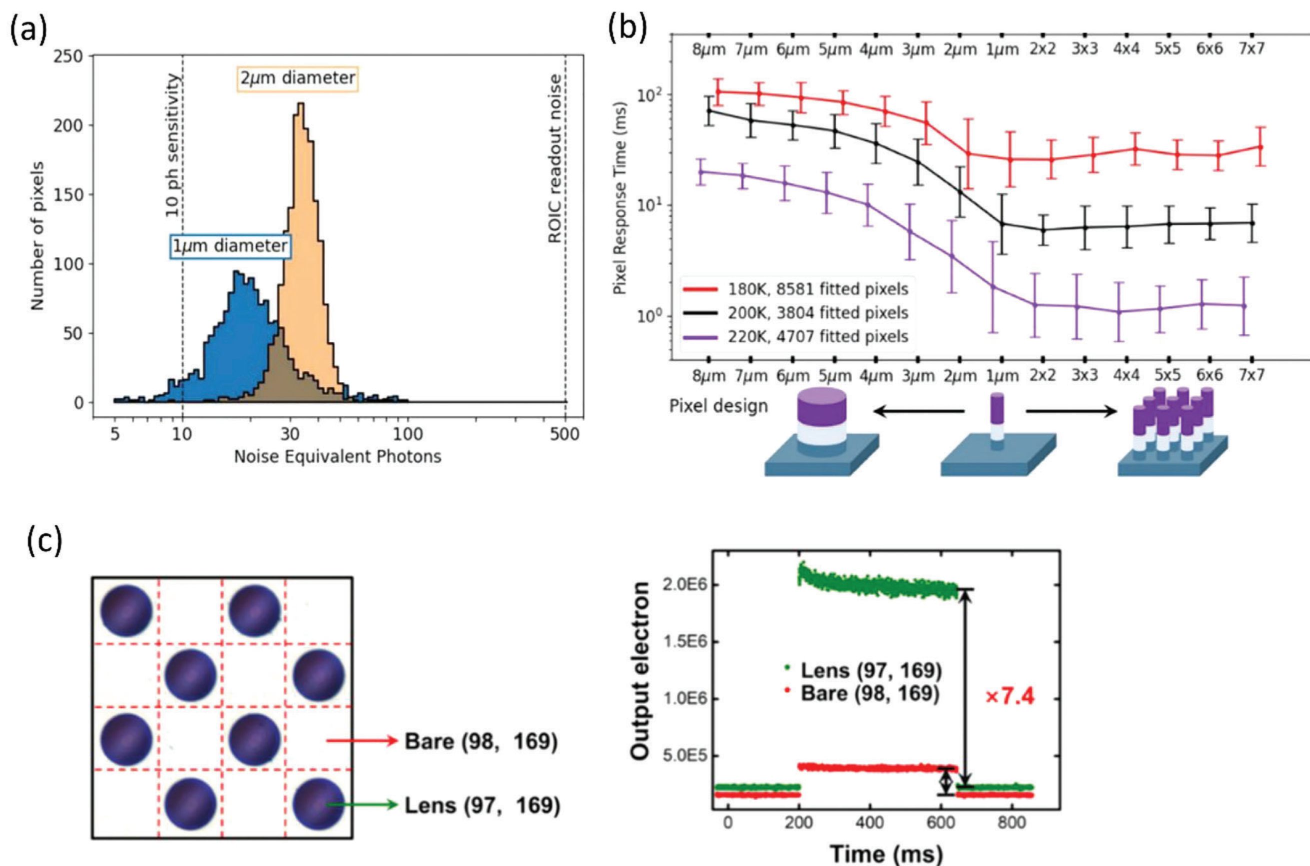

Figure 19. a) Histograms of NEPh of pixels of different sizes. Note that the higher spread in 1 μm histogram can be attributed to the process variations. Reproduced with permission.[15] Copytight 2020, AIP Publishing. b) Response time distribution for multi-pillar and single-pillar pixels of different sizes. As can be seen, all multi-pillar pixels have similar response times regardless of the number of pillars. Reproduced with permission.[27] Copyright 2022, American Chemical Society. c) Checkered design of the micro lens array on a camera allows to quantify the 7.4 response improvement factor enabled by the micro lenses. Reproduced with permission.[103] Copyright 2022, American Chemical Society.

theoretical model. Histograms of noise-equivalent photon sensitivity (NEPh) of these devices at different temperatures clearly validated the theoretical model with a very high statistical confidence (**Figure 19**a).

Similarly, we used this ROIC-based high throughput measurement approach to study different methods for increasing the quantum efficiency of nano-photodetectors.[27] A large number of different device types were fabricated side-by-side on a ROIC. Another theoretical model we developed suggested that an array of connected small phototransistors could be more sensitive than a single large device with the same overall area. We wanted to experimentally test this model with high statistical confidence. We integrated a large number of arrays, each made of a set of devices with different diameters and a set of devices with different number of connected 1 μm diameter devices (from 1 to 49 connected devices forming one pixel). Statistical comparison of the response time of these devices at different temperatures showed an interesting trend: regardless of the number of connected 1 um devices, the response time stays the same (Figure 19b). In contrast to increasing the diameter of the device, by adding more connected small devices, a larger photo-sensitive area is produced without a decrease in the speed of the device as predicted by the theoretical model.

This ROIC-based high-throughput method does not need to be limited to the photodetector evaluation and could also be used to evaluate other features. For example, we developed a new method of fabricating an array of solid-immersion micro-lenses directly on our focal-plane arrays to improve the fill factor of nano-photodetector devices.[103] To provide an accurate evaluation of the effect of the immersion lens array on the response of the detectors, each lensed detector on this array is surrounded by four bare reference detectors in a checkered pattern. These bare detectors provide the means for accurate comparison of the enhancement of device response due to the microlenses (Figure 19c).

5. Summary and Outlook

In this article, new photodetectors based on low-dimensional materials and reports on their integration on silicon CMOS chips were reviewed. Methods for creating and testing high-resolution and high-performance imaging sensors based on low-dimensional materials were also presented. In addition, major technical barriers against the widespread use of low-dimensional materials in image sensors were discussed and some promising solutions were evaluated.

© 2023 The Authors. Small Methods published by Wiley-VCH GmbH

23669608, 0, Downloaded from https://onlinelibrary.wiley.com/doi/10.1002/smtd.202300595 by Northwestern University Libraries, Wiley Online Library on [14/11/2023]. See the Terms and Conditions (https://onlinelibrary.wiley.com/terms-and-conditions) on Wiley Online Library for rules of use; OA articles are governed by the applicable Creative Commons License

The historic development of semiconductor-based imaging arrays has had a massive impact on many aspects of our lives. While silicon has been the backbone of imaging chips, its limitations prompted heterogeneous integration of different material on silicon almost immediately after the first silicon imaging arrays were invented. Despite the colossal progresses made in this field, the inherent properties of bulk and epitaxially grown semiconductors have limited advancements in some of the most desirable directions, such as in-pixel computing and multi-band imaging. We believe that the unique properties of low-dimensional materials, such as low capacitance, stackability, programmability, and mechanical flexibility, could be used to make imagers with unprecedented performance. Most notably, the field of bio-inspired imaging substantially benefits from these properties and its commercial implementation may finally be within our reach.

Acknowledgements

S.A., S.B., and C.-M.K. contributed equally to this work. H.M. defined the scope of the review and contributed to all sections. The research was carried out in part at the Jet Propulsion Laboratory, California Institute of Technology, under a contract with the National Aeronautics and Space Administration (80NM0018D0004).

Conflict of Interest

The authors declare no conflict of interest.

Keywords

bio-inspired imaging, CMOS readout integrated circuits, infrared cameras, low-dimensional materials, photodetectors, single-photon detectors

Received: May 8, 2023
Revised: June 25, 2023
Published online:

[1] Chart: More Phones Than People | Statista, https://www.statista.com/chart/4022/mobile-subscriptions-and-world-population/ (accessed: June 2023).
[2] A. Rogalski, *Opto-Electron. Rev.* **2012**, *20*, 279.
[3] A. Glushkova, P. Andričević, R. Smajda, B. Náfrádi, M. Kollár, V. Djokić, A. Arakcheeva, L. Forró, R. Pugin, E. Horváth, *ACS Nano* **2021**, *15*, 4077.
[4] X.-X. Li, G. Zeng, Y.-C. Li, H. Zhang, Z.-G. Ji, Y.-G. Yang, M. Luo, W.-D. Hu, D. W. Zhang, H.-L. Lu, *npj Flexible Electron.* **2022**, *6*, 47.
[5] W.-H. Chen, C.-H. Ma, S.-H. Hsieh, Y.-H. Lai, Y.-C. Kuo, C.-H. Chen, S.-P. Chang, S.-J. Chang, R.-H. Horng, Y.-H. Chu, *ACS Appl. Electron. Mater.* **2022**, *4*, 3099.
[6] J.-M. Choi, H. Y. Jang, A. R. Kim, J.-D. Kwon, B. Cho, M. H. Park, Y. Kim, *Nanoscale* **2021**, *13*, 672.
[7] J. Yin, Z. Tan, H. Hong, J. Wu, H. Yuan, Y. Liu, C. Chen, C. Tan, F. Yao, T. Li, Y. Chen, Z. Liu, K. Liu, H. Peng, *Nat. Commun.* **2018**, *9*, 3311.
[8] X. Yang, A. Vorobiev, J. Yang, K. Jeppson, J. Stake, *IEEE Trans. Terahertz Sci. Technol.* **2020**, *10*, 554.
[9] X. Yang, A. Vorobiev, A. Generalov, M. A. Andersson, J. Stake, *Appl. Phys. Lett.* **2017**, *111*, 021102.
[10] P. Ajayan, P. Kim, K. Banerjee, *Phys. Today* **2016**, *69*, 38.
[11] J. N. Tinsley, M. I. Molodtsov, R. Prevedel, D. Wartmann, J. Espigulé-Pons, M. Lauwers, A. Vaziri, *Nat. Commun.* **2016**, *7*, 12172.
[12] P. Dudek, T. Richardson, L. Bose, S. Carey, J. Chen, C. Greatwood, Y. Liu, W. Mayol-Cuevas, *Sci. Robot.* **2022**, *7*, 7755.
[13] M. Rezaei, M.-S. Park, C. L. Tan, H. Mohseni, *IEEE Electron. Device Lett.* **2017**, *38*, 1051.
[14] M. Rezaei, S. Bianconi, L. J. Lauhon, H. Mohseni, *Nano Lett.* **2021**, *21*, 9838.
[15] L. Liu, J. Rabinowitz, S. Bianconi, M.-S. Park, H. Mohseni, *Appl. Phys. Lett.* **2020**, *117*, 191102.
[16] M. Bernardi, C. Ataca, M. Palummo, J. C. Grossman, *Nanophotonics* **2017**, *6*, 479.
[17] A. Altaqui, P. Sen, H. Schrickx, J. Rech, J.-W. Lee, M. Escuti, W. You, B. J. Kim, R. Kolbas, B. T. O'Connor, M. Kudenov, *Sci. Adv.* **2021**, *7*, 3196.
[18] M. Garcia, C. Edmiston, R. Marinov, A. Vail, V. Gruev, *Optica* **2017**, *4*, 1263.
[19] T. Nagata, M. Koyanagi, H. Tsukamoto, S. Saeki, K. Isono, Y. Shichida, F. Tokunaga, M. Kinoshita, K. Arikawa, A. Terakita, *Science* **2012**, *335*, 469.
[20] M.-B. Lien, C.-H. Liu, I. Y. Chun, S. Ravishankar, H. Nien, M. Zhou, J. A. Fessler, Z. Zhong, T. B. Norris, *Nat. Photonics* **2020**, *14*, 143.
[21] S.-B. Rim, P. B. Catrysse, R. Dinyari, K. Huang, P. Peumans, *Opt. Express* **2008**, *16*, 4965.
[22] B. Guenter, N. Joshi, R. Stoakley, A. Keefe, K. Geary, R. Freeman, J. Hundley, P. Patterson, D. Hammon, G. Herrera, E. Sherman, A. Nowak, R. Schubert, P. Brewer, L. Yang, R. Mott, G. McKnight, *Opt. Express* **2017**, *25*, 13010.
[23] M. A. Mahowald, C. Mead, *Sci. Am.* **1991**, 76.
[24] D. H. Hubel, T. N. Wiesel, *J Physiol* **1962**, *160*, 106.
[25] L. Britnell, R. M. Ribeiro, A. Eckmann, R. Jalil, B. D. Belle, A. Mishchenko, Y.-J. Kim, R. V. Gorbachev, T. Georgiou, S. V. Morozov, A. N. Grigorenko, A. K. Geim, C. Casiraghi, A. H. C. Neto, K. S. Novoselov, *Science* **2013**, *340*, 1311.
[26] L. Kuo, V. K. Sangwan, S. V. Rangnekar, T. Chu, D. Lam, Z. Zhu, L. J. Richter, R. Li, B. M. Szydłowska, J. R. Downing, B. J. Luijten, L. J. Lauhon, M. C. Hersam, *Adv. Mater.* **2022**, *34*, 2203772.
[27] S. Bianconi, J. Rabinowitz, C.-M. Kang, L. Liu, M. Rezaei, H. Nawaz, H. Mohseni, *ACS Photonics* **2022**, *9*, 2280.
[28] H. Xu, B. Ding, Y. Xu, Z. Huang, D. Wei, S. Chen, T. Lan, Y. Pan, H.-M. Cheng, B. Liu, *Nat. Nanotechnol.* **2022**, *17*, 1091.
[29] N. Liu, H. Tian, G. Schwartz, J. B.-H. Tok, T.-L. Ren, Z. Bao, *Nano Lett.* **2014**, *14*, 3702.
[30] S. Goossens, G. Navickaite, C. Monasterio, S. Gupta, J. J. Piqueras, R. Pérez, G. Burwell, I. Nikitskiy, T. Lasanta, T. Galán, E. Puma, A. Centeno, A. Pesquera, A. Zurutuza, G. Konstantatos, F. Koppens, *Nat. Photonics* **2017**, *11*, 366.
[31] L. Tong, X. Huang, P. Wang, L. Ye, M. Peng, L. An, Q. Sun, Y. Zhang, G. Yang, Z. Li, F. Zhong, F. Wang, Y. Wang, M. Motlag, W. Wu, G. J. Cheng, W. Hu, *Nat. Commun.* **2020**, *11*, 2308.
[32] M. Peng, R. Xie, Z. Wang, P. Wang, F. Wang, H. Ge, Y. Wang, F. Zhong, P. Wu, J. Ye, Q. Li, L. Zhang, X. Ge, Y. Ye, Y. Lei, W. Jiang, Z. Hu, F. Wu, X. Zhou, J. Miao, J. Wang, H. Yan, C. Shan, J. Dai, C. Chen, X. Chen, W. Lu, W. Hu, *Sci. Adv.* **2021**, *7*, 7358.
[33] Y. Zhang, L. Huang, J. Li, Z. Dong, Q. Yu, T. Lei, C. Chen, L. Yang, Y. Dai, J. Zhang, W. Yu, Q. Bao, K. Zhang, *Appl. Phys. Lett.* **2022**, *120*, 261101.
[34] A. Hwang, M. Park, Y. Park, Y. Shim, S. Youn, C.-H. Lee, H. B. Jeong, H. Y. Jeong, J. Chang, K. Lee, G. Yoo, J. Heo, *Sci. Adv.* **2021**, *7*, 2521.
[35] T.-Y. Chang, P.-L. Chen, P.-S. Chen, W.-Q. Li, J.-X. Li, M.-Y. He, J.-T. Chao, C.-H. Ho, C.-H. Liu, *ACS Appl. Mater. Interfaces* **2022**, *14*, 32665.

© 2023 The Authors. Small Methods published by Wiley-VCH GmbH

23669608, 0, Downloaded from https://onlinelibrary.wiley.com/doi/10.1002/smtd.202300595 by Northwestern University Libraries, Wiley Online Library on [14/11/2023]. See the Terms and Conditions (https://onlinelibrary.wiley.com/terms-and-conditions) on Wiley Online Library for rules of use; OA articles are governed by the applicable Creative Commons License

[36] P. Wu, L. Ye, L. Tong, P. Wang, Y. Wang, H. Wang, H. Ge, Z. Wang, Y. Gu, K. Zhang, Y. Yu, M. Peng, F. Wang, M. Huang, P. Zhou, W. Hu, *Light Sci. Appl.* **2022**, *11*, 6.
[37] A. Castellanos-Gomez, *Nat. Photonics* **2016**, *10*, 202.
[38] S. G. Seo, S. Y. Kim, J. Jeong, S. H. Jin, *Nano Res.* **2021**, *14*, 2938.
[39] A. Jana, S. Cho, S. A. Patil, A. Meena, Y. Jo, V. G. Sree, Y. Park, H. Kim, H. Im, R. A. Taylor, *Mater. Today* **2022**, *55*, 110.
[40] S. Cheng, M. Nikl, A. Beitlerova, R. Kucerkova, X. Du, G. Niu, Y. Jia, J. Tang, G. Ren, Y. Wu, *Adv. Opt. Mater.* **2021**, *9*, 2100460.
[41] S. Cheng, A. Beitlerova, R. Kucerkova, M. Nikl, G. Ren, Y. Wu, *Phys. Status Solidi Rapid Res. Lett.* **2020**, *14*, 2000374.
[42] F. Zhou, Z. Li, W. Lan, Q. Wang, L. Ding, Z. Jin, *Small Methods* **2020**, *4*, 2000506.
[43] Y. He, I. Hadar, M. G. Kanatzidis, *Nat. Photonics* **2022**, *16*, 14.
[44] D.-G. Kim, S. Han, J. Hwang, I. H. Do, D. Jeong, J.-H. Lim, Y.-H. Lee, M. Choi, Y.-H. Lee, D.-Y. Choi, H. Lee, *Nat. Commun.* **2020**, *11*, 5933.
[45] D. A. Fishman, C. M. Cirloganu, S. Webster, L. A. Padilha, M. Monroe, D. J. Hagan, E. W. Van Stryland, *Nat. Photonics* **2011**, *5*, 561.
[46] D. Knez, A. M. Hanninen, R. C. Prince, E. O. Potma, D. A. Fishman, *Light Sci. Appl.* **2020**, *9*, 125.
[47] J. Wang, C. Jiang, W. Li, X. Xiao, *Adv. Opt. Mater.* **2022**, *10*, 2102436.
[48] N. Li, Z. Lan, Y. S. Lau, J. Xie, D. Zhao, F. Zhu, *Adv. Sci.* **2020**, *7*, 200044.
[49] H. Mohseni, Hooman Mohseni, *US 9472597*, **2016**.
[50] S.-J. He, D.-K. Wang, Z.-X. Yang, J.-X. Man, Z.-H. Lu, *Appl. Phys. Lett.* **2018**, *112*, 243301
[51] D. Yang, X. Zhou, D. Ma, A. Vadim, T. Ahamad, S. M. Alshehri, *Mater. Horiz.* **2018**, *5*, 874.
[52] H. Yu, D. Kim, J. Lee, S. Baek, J. Lee, R. Singh, F. So, *Nat. Photonics* **2016**, *10*, 129.
[53] Y. M. Chi, A. Abbas, S. Chakrabartty, G. Cauwenberghs, in *2009 IEEE Int. Symp. on Circuits and Systems*, IEEE, Taipei, Taiwan **2009**.
[54] Y. M. Chi, U. Mallik, M. A. Clapp, E. Choi, G. Cauwenberghs, R. Etienne-Cummings, *IEEE J. Solid-State Circuits* **2007**, *42*, 2187.
[55] R. Kubendran, A. Paul, G. Cauwenberghs, in *2021 IEEE Custom Integrated Circuits Conf. (CICC)*, IEEE, Austin, TX **2021**.
[56] G. Cauwenberghs, *Proc. Natl. Acad. Sci. USA* **2013**, *110*, 15512.
[57] V. K. Sangwan, H.-S. Lee, H. Bergeron, I. Balla, M. E. Beck, K.-S. Chen, M. C. Hersam, *Nature* **2018**, *554*, 500.
[58] G. Ding, B. Yang, R. Chen, W. Mo, K. Zhou, Y. Liu, G. Shang, Y. Zhai, S. Han, Y. Zhou, *Small* **2021**, *17*, 2103175.
[59] X. Yan, J. H. Qian, V. K. Sangwan, M. C. Hersam, *Adv. Mater.* **2022**, *34*, 2108025.
[60] L. Wang, W. Liao, S. L. Wong, Z. G. Yu, S. Li, Y. Lim, X. Feng, W. C. Tan, X. Huang, L. Chen, L. Liu, J. Chen, X. Gong, C. Zhu, X. Liu, Y. Zhang, D. Chi, K. Ang, *Adv. Funct. Mater.* **2019**, *29*, 1901106.
[61] D. Jayachandran, A. Pannone, M. Das, T. F. Schranghamer, D. Sen, S. Das, *ACS Nano* **2022**, *17*, 1068.
[62] A. Dodda, N. Trainor, Joan. M. Redwing, S. Das, *Nat. Commun.* **2022**, *13*, 3587.
[63] M. Dubreuil, P. Delrot, I. Leonard, A. Alfalou, C. Brosseau, A. Dogariu, *Appl. Opt.* **2013**, *52*, 997.
[64] P. Soffitta, X. Barcons, R. Bellazzini, J. Braga, E. Costa, G. W. Fraser, S. Gburek, J. Huovelin, G. Matt, M. Pearce, J. Poutanen, V. Reglero, A. Santangelo, R. A. Sunyaev, G. Tagliaferri, M. Weisskopf, R. Aloisio, E. Amato, P. Attiná, M. Axelsson, L. Baldini, S. Basso, S. Bianchi, P. Blasi, J. Bregeon, A. Brez, N. Bucciantini, L. Burderi, V. Burwitz, P. Casella, et al., *Exp. Astron. (Dordr)* **2013**, *36*, 523.
[65] K. Kinoshita, R. Moriya, M. Onodera, Y. Wakafuji, S. Masubuchi, K. Watanabe, T. Taniguchi, T. Machida, *npj 2D Mater. Appl.* **2019**, *3*, 22.
[66] J. S. Tyo, D. L. Goldstein, D. B. Chenault, J. A. Shaw, *Appl. Opt.* **2006**, *45*, 5453.
[67] W. Yang, J. Yang, K. Zhao, Q. Gao, L. Liu, Z. Zhou, S. Hou, X. Wang, G. Shen, X. Pang, Q. Xu, Z. Wei, *Adv. Sci.* **2021**, *8*, 2100075.
[68] H. Yang, H. Jussila, A. Autere, H.-P. Komsa, G. Ye, X. Chen, T. Hasan, Z. Sun, *ACS Photonics* **2017**, *4*, 3023.
[69] L. Gao, K. Zeng, J. Guo, C. Ge, J. Du, Y. Zhao, C. Chen, H. Deng, Y. He, H. Song, G. Niu, J. Tang, *Nano Lett.* **2016**, *16*, 7446.
[70] S. Zhang, C. Bi, T. Qin, Y. Liu, J. Cao, J. Song, Y. Huo, M. Chen, Q. Hao, X. Tang, *ACS Photonics* **2023**, *10*, 673.
[71] J. Jean, J. Xiao, R. Nick, N. Moody, M. Nasilowski, M. Bawendi, V. Bulović, *Energy Environ. Sci.* **2018**, *11*, 2295.
[72] J. An, B. Wang, C. Shu, W. Wu, B. Sun, Z. Zhang, D. Li, S. Li, *Nano Select* **2021**, *2*, 527.
[73] K. S. Novoselov, A. K. Geim, S. V. Morozov, D. Jiang, Y. Zhang, S. V. Dubonos, I. V. Grigorieva, A. A. Firsov, *Science* **2004**, *306*, 666.
[74] X. Li, L. Tao, Z. Chen, H. Fang, X. Li, X. Wang, J.-B. Xu, H. Zhu, *Appl. Phys. Rev.* **2017**, *4*, 021306.
[75] K. S. Novoselov, V. I. Fal′ko, L. Colombo, P. R. Gellert, M. G. Schwab, K. Kim, *Nature* **2012**, *490*, 192.
[76] A. K. Geim, K. S. Novoselov, *Nat. Mater.* **2007**, *6*, 183.
[77] S. Ullah, X. Yang, H. Q. Ta, M. Hasan, A. Bachmatiuk, K. Tokarska, B. Trzebicka, L. Fu, M. H. Rummeli, *Nano Res.* **2021**, *14*, 3756.
[78] I. Song, Y. Park, H. Cho, H. C. Choi, *Angew. Chem., Int. Ed.* **2018**, *57*, 15374.
[79] Y. Dong, Y. Xie, C. Xu, Y. Fu, X. Fan, X. Li, L. Wang, F. Xiong, W. Guo, G. Pan, Q. Wang, F. Qian, J. Sun, *Nanotechnology* **2018**, *29*, 365301.
[80] B. G. Shin, D. H. Boo, B. Song, S. Jeon, M. Kim, S. Park, E. S. An, J. S. Kim, Y. J. Song, Y. H. Lee, *ACS Nano* **2019**, *13*, 6662.
[81] Y. Shi, H. Li, L.-J. Li, *Chem. Soc. Rev.* **2015**, *44*, 2744.
[82] Z. Li, P. Wu, C. Wang, X. Fan, W. Zhang, X. Zhai, C. Zeng, Z. Li, J. Yang, J. Hou, *ACS Nano* **2011**, *5*, 3385.
[83] T. Jurca, M. J. Moody, A. Henning, J. D. Emery, B. Wang, J. M. Tan, T. L. Lohr, L. J. Lauhon, T. J. Marks, *Angew. Chem., Int. Ed.* **2017**, *56*, 4991.
[84] B. Qin, H. Ma, M. Hossain, M. Zhong, Q. Xia, B. Li, X. Duan, *Chem. Mater.* **2020**, *32*, 10321.
[85] A. J. Watson, W. Lu, M. H. D. Guimarães, M. Stöhr, *2D Mater.* **2021**, *8*, 032001.
[86] R. Mupparapu, T. Bucher, I. Staude, *Adv. Phys. X* **2020**, *5*, 1734083.
[87] H. Jia, R. Yang, A. E. Nguyen, S. N. Alvillar, T. Empante, L. Bartels, P. X.-L. Feng, *Nanoscale* **2016**, *8*, 10677.
[88] M.-A. Kang, S. J. Kim, W. Song, S. Chang, C.-Y. Park, S. Myung, J. Lim, S. S. Lee, K.-S. An, *Carbon N Y* **2017**, *116*, 167.
[89] M. Amani, M. L. Chin, A. L. Mazzoni, R. A. Burke, S. Najmaei, P. M. Ajayan, J. Lou, M. Dubey, *Appl. Phys. Lett.* **2014**, *104*, 203506.
[90] L. Zhang, C. Wang, X.-L. Liu, T. Xu, M. Long, E. Liu, C. Pan, G. Su, J. Zeng, Y. Fu, Y. Wang, Z. Yan, A. Gao, K. Xu, P.-H. Tan, L. Sun, Z. Wang, X. Cui, F. Miao, *Nanoscale* **2017**, *9*, 19124.
[91] T. Zhang, K. Fujisawa, T. Granzier-Nakajima, F. Zhang, Z. Lin, E. Kahn, N. Perea-López, A. L. Elías, Y.-T. Yeh, M. Terrones, *ACS Appl. Nano Mater.* **2019**, *2*, 5320.
[92] A. Castellanos-Gomez, M. Buscema, R. Molenaar, V. Singh, L. Janssen, H. S. J. van der Zant, G. A. Steele, *2D Mater.* **2014**, *1*, 011002.
[93] A. Gurarslan, Y. Yu, L. Su, Y. Yu, F. Suarez, S. Yao, Y. Zhu, M. Ozturk, Y. Zhang, L. Cao, *ACS Nano* **2014**, *8*, 11522.
[94] Z.-Q. Xu, Y. Zhang, S. Lin, C. Zheng, Y. L. Zhong, X. Xia, Z. Li, P. J. Sophia, M. S. Fuhrer, Y.-B. Cheng, Q. Bao, *ACS Nano* **2015**, *9*, 6178.
[95] Y.-C. Lin, C. Jin, J.-C. Lee, S.-F. Jen, K. Suenaga, P.-W. Chiu, *ACS Nano* **2011**, *5*, 2362.
[96] Z. Lin, Y. Zhao, C. Zhou, R. Zhong, X. Wang, Y. H. Tsang, Y. Chai, *Sci. Rep.* **2015**, *5*, 18596.
[97] L. Kou, C. Chen, S. C. Smith, *J. Phys. Chem. Lett.* **2015**, *5*, 2794.
[98] J. R. Brent, N. Savjani, E. A. Lewis, S. J. Haigh, D. J. Lewis, P. O'Brien, *Chem. Commun.* **2014**, *50*, 13338.

 © 2023 The Authors. Small Methods published by Wiley-VCH GmbH

23669608, 0, Downloaded from https://onlinelibrary.wiley.com/doi/10.1002/smtd.202300595 by Northwestern University Libraries, Wiley Online Library on [14/11/2023]. See the Terms and Conditions (https://onlinelibrary.wiley.com/terms-and-conditions) on Wiley Online Library for rules of use; OA articles are governed by the applicable Creative Commons License

[99] D. Hanlon, C. Backes, E. Doherty, C. S. Cucinotta, N. C. Berner, C. Boland, K. Lee, A. Harvey, P. Lynch, Z. Gholamvand, S. Zhang, K. Wang, G. Moynihan, A. Pokle, Q. M. Ramasse, N. McEvoy, W. J. Blau, J. Wang, G. Abellan, F. Hauke, A. Hirsch, S. Sanvito, D. D. O'Regan, G. S. Duesberg, V. Nicolosi, J. N. Coleman, *Nat. Commun.* **2015**, *6*, 8563.
[100] P. Yasaei, B. Kumar, T. Foroozan, C. Wang, M. Asadi, D. Tuschel, J. E. Indacochea, R. F. Klie, A. Salehi-Khojin, *Adv. Mater.* **2015**, *27*, 1887.
[101] F. Bonaccorso, Z. Sun, T. Hasan, A. C. Ferrari, *Nat. Photonics* **2010**, *4*, 611.
[102] D. J. Merthe, V. V. Kresin, *Phys. Rev. B* **2016**, *94*, 259439.
[103] C.-M. Kang, S. Bianconi, T. Hamilton, J. Rabinowitz, S. Wheaton, L. Liu, M. Ulmer, H. Mohseni, *ACS Appl. Electron. Mater.* **2022**, *4*, 1910.
[104] S. Zhang, A. Soibel, S. A. Keo, D. Wilson, Sir. B. Rafol, D. Z. Ting, A. She, S. D. Gunapala, F. Capasso, *Appl. Phys. Lett.* **2018**, *113*, 111104.
[105] S. A. Maier, *Plasmonics: Fundamentals and Applications*, **2007**.
[106] A. Belahmar, A. Chouiyakh, M. Fahoume, *OAlib* **2017**, *4*, 1.
[107] Y. Nishijima, L. Rosa, S. Juodkazis, *Opt. Express* **2012**, *20*, 11466.
[108] G. X. Ni, A. S. McLeod, Z. Sun, L. Wang, L. Xiong, K. W. Post, S. S. Sunku, B.-Y. Jiang, J. Hone, C. R. Dean, M. M. Fogler, D. N. Basov, *Nature* **2018**, *557*, 530.
[109] W.-S. Chang, B. A. Willingham, L. S. Slaughter, B. P. Khanal, L. Vigderman, E. R. Zubarev, S. Link, *Proc. Natl. Acad. Sci. USA* **2011**, *108*, 19879.
[110] S. Y. Chou, P. R. Krauss, P. J. Renstrom, *Science* **1996**, *272*, 85.
[111] A. Bonakdar, M. Rezaei, R. L. Brown, V. Fathipour, E. Dexheimer, S. J. Jang, H. Mohseni, *Opt. Lett.* **2015**, *40*, 2537.
[112] A. Bonakdar, M. Rezaei, E. Dexheimer, H. Mohseni, *Nanotechnology* **2016**, *27*, 035301.
[113] N. Youngblood, C. Chen, S. J. Koester, M. Li, *Nat. Photonics* **2015**, *9*, 247.
[114] H. Lin, Y. Song, Y. Huang, D. Kita, S. Deckoff-Jones, K. Wang, L. Li, J. Li, H. Zheng, Z. Luo, H. Wang, S. Novak, A. Yadav, C.-C. Huang, R.-J. Shiue, D. Englund, T. Gu, D. Hewak, K. Richardson, J. Kong, J. Hu, *Nat. Photonics* **2017**, *11*, 798.
[115] J. T. Kim, Y.-J. Yu, H. Choi, C.-G. Choi, *Opt. Express* **2014**, *22*, 803.
[116] Y. Ding, Z. Cheng, X. Zhu, K. Yvind, J. Dong, M. Galili, H. Hu, N. A. Mortensen, S. Xiao, L. K. Oxenløwe, *Nanophotonics* **2020**, *9*, 317.
[117] M. Engel, M. Steiner, A. Lombardo, A. C. Ferrari, H. v. Löhneysen, P. Avouris, R. Krupke, *Nat. Commun.* **2012**, *3*, 906.
[118] M. Furchi, A. Urich, A. Pospischil, G. Lilley, K. Unterrainer, H. Detz, P. Klang, A. M. Andrews, W. Schrenk, G. Strasser, T. Mueller, *Nano Lett.* **2012**, *7*, 2773.
[119] R.-J. Shiue, X. Gan, Y. Gao, L. Li, X. Yao, A. Szep, D. Walker, J. Hone, D. Englund, *Appl. Phys. Lett.* **2013**, *103*, 241109.
[120] L. Xiong, C. Forsythe, M. Jung, A. S. McLeod, S. S. Sunku, Y. M. Shao, G. X. Ni, A. J. Sternbach, S. Liu, J. H. Edgar, E. J. Mele, M. M. Fogler, G. Shvets, C. R. Dean, D. N. Basov, *Nat. Commun.* **2019**, *10*, 4780.
[121] A. Bonakdar, H. Mohseni, *Opt. Lett.* **2013**, *38*, 2726.
[122] S. Bianconi, L. J. Lauhon, H. Mohseni, *Nat. Photonics* **2021**, *15*, 714.
[123] A. van der Ziel, *Proc. IEEE* **1970**, *58*, 1178.
[124] K. M. van Vliet, *Appl. Opt.* **1967**, *6*, 1145.
[125] F. Wang, T. Zhang, R. Xie, Z. Wang, W. Hu, *Nat. Commun.* **2023**, *14*, 2224.
[126] Y. Fang, A. Armin, P. Meredith, J. Huang, *Nat. Photonics* **2019**, *13*, 1.
[127] Z. Bielecki, K. Achtenberg, M. Kopytko, J. Mikołajczyk, J. Wojtas, A. Rogalski, *Bull. Polish Acad. Sci. Tech. Sci.* **2022**, *70*, 140534.
[128] S. Bianconi, H. Mohseni, *Rep. Prog. Phys.* **2020**, *83*, 044101.
[129] A. Rogalski, *Infrared Detectors*, 2nd ed, CRC Press, London **2010**.
[130] H. T. Friis, *Proc. IRE* **1944**, *32*, 419.
[131] H. Spieler, *Semiconductor Detector Systems*, Oxford University Press, Oxford **2005**.
[132] J.-R. Riba, F. Capelli, *Energies (Basel)* **2018**, *11*, 1090.
[133] E. Sczygelski, V. K. Sangwan, C.-C. Wu, H. N. Arnold, K. Everaerts, T. J. Marks, M. C. Hersam, L. J. Lauhon, *Appl. Phys. Lett.* **2013**, *102*, 083104.
[134] Y. Qin, R. Yang, Z. L. Wang, *J. Phys. Chem. C* **2008**, *112*, 18734.
[135] Y. Zhang, J. Wang, H. Zhu, H. Li, L. Jiang, C. Shu, W. Hu, C. Wang, *J. Mater. Chem.* **2010**, *20*, 9858.
[136] W. Xiong, J.-W. Wang, W.-J. Fan, Z.-G. Song, C.-S. Tan, *Sci. Rep.* **2020**, *20*, 9858.
[137] J. Jadwiszczak, D. Keane, P. Maguire, C. P. Cullen, Y. Zhou, H. Song, C. Downing, D. Fox, N. McEvoy, R. Zhu, J. Xu, G. S. Duesberg, Z.-M. Liao, J. J. Boland, H. Zhang, *ACS Nano* **2019**, *13*, 14262.
[138] Y. Zou, Z. Zhang, J. Yan, L. Lin, G. Huang, Y. Tan, Z. You, P. Li, *Nat. Commun.* **2022**, *13*, 4372.
[139] B. H. Kim, H. Yoon, S. H. Kwon, D. W. Kim, Y. J. Yoon, *Vacuum* **2021**, *184*, 109950.
[140] P. Wang, S. Liu, W. Luo, H. Fang, F. Gong, N. Guo, Z.-G. Chen, J. Zou, Y. Huang, X. Zhou, J. Wang, X. Chen, W. Lu, F. Xiu, W. Hu, *Adv. Mater.* **2017**, *29*, 1604439.
[141] K. Thakar, B. Mukherjee, S. Grover, N. Kaushik, M. Deshmukh, S. Lodha, *ACS Appl. Mater. Interfaces* **2018**, *10*, 36512.
[142] T. J. Octon, V. K. Nagareddy, S. Russo, M. F. Craciun, C. D. Wright, *Adv. Opt. Mater.* **2016**, *4*, 1750.
[143] Y. Zhao, C. Li, J. Jiang, B. Wang, L. Shen, *Small* **2020**, *16*, 2001534.
[144] Q. Xu, J. Wang, W. Shao, X. Ouyang, X. Wang, X. Zhang, Y. Guo, X. Ouyang, *Nanoscale* **2020**, *12*, 9727.
[145] P. Ehrett, V. Goyal, O. Matthews, R. Das, T. Austin, V. Bertacco. UMich. Ann Arbor Tech. Rep. CSE-TR-002-17, **2017**.
[146] B. Fièque, L. Martineau, E. Sanson, P. Chorier, O. Boulade, V. Moreau, H. Geoffray, Proceedings Volume 8176, Sensors, Systems, and Next-Generation Satellites XV, SPIE Remote Sensing, Prague, Czech Republic **2011**, https://doi.org/10.1117/12.898987.
[147] A. Joshi, J. Stevens, A. Kononenko, J. Blackwell, Proceedings Volume 5499, Optical and Infrared Detectors for Astronomy, SPIE Astronomical Telescopes + Instrumentation, Glasgow, United Kingdom **2004**, https://doi.org/10.1117/12.551062.
[148] D. D. L. Chung, *J. Mater. Eng. Perform.* **2000**, *9*, 350.
[149] M. W. Glasscott, E. W. Brown, K. Dorsey, C. H. Laber, K. Conley, J. D. Ray, L. C. Moores, A. Netchaev, *Anal. Chem.* **2022**, *94*, 11983.
[150] F. E. Terman, *Radio Engineer's Handbook*, McGraw-Hill Book Company, Inc, New York **1943**.
[151] C. A. Balanis, *Antenna Theory: Analysis and Design*, 4th ed., John Wiley and Sons **2016**, p. 110.
[152] J. Liu, P. Liu, D. Chen, T. Shi, X. Qu, L. Chen, T. Wu, J. Ke, K. Xiong, M. Li, H. Song, W. Wei, J. Cao, J. Zhang, L. Gao, J. Tang, *Nat. Electron.* **2022**, *5*, 443.

© 2023 The Authors. Small Methods published by Wiley-VCH GmbH

23669608, 0, Downloaded from https://onlinelibrary.wiley.com/doi/10.1002/smtd.202300595 by Northwestern University Libraries, Wiley Online Library on [14/11/2023]. See the Terms and Conditions (https://onlinelibrary.wiley.com/terms-and-conditions) on Wiley Online Library for rules of use; OA articles are governed by the applicable Creative Commons License

Samaneh Ansari received her B.S. degree from Sharif University of Technology, Tehran. She is a Ph.D. student in Mohseni Lab at Northwestern University, where she received a Murphy Fellowship. Her research interests are simulation, fabrication, and characterization of III–V photodetectors.

Simone Bianconi obtained a Bachelor and a Master degree from the University of Bologna, Italy, and he earned a Ph.D. from Northwestern University in 2021, with a thesis on innovative devices and materials for infrared sensing and imaging which received the departmental best thesis award. He is currently an MDL next postdoctoral fellow at the Microdevices Laboratory at Jet Propulsion Laboratory, where his research focuses on a range of different remote sensing techniques, including direct imaging, LIDAR and quantum sensing. He was a Ryan fellow of the International Institute of Nanotechnology.

Chang-Mo Kang received Ph.D. degree from Gwangju Institute of Science and Technology (GIST), South Korea, 2018. He worked at Mohseni Lab at Northwestern University as a post-doctoral researcher from 2018 to 2021. He joined Korea Photonics Technology Institute (KOPTI), South Korea in 2021. He is currently a senior researcher at Photonic Semiconductor Research Center, KOPTI. His current research interests include compound semiconductors, micro-LED displays, and infrared image sensors.

Hooman Mohseni is the AT&T chair professor of electrical and computer engineering, and professor of physics and astronomy, at Northwestern University. He is the recipient of several research and teaching awards including W.M. Keck Foundation Award, NSF CAREER Award, DARPA Young Faculty Award, and Northwestern Faculty Honor Roll. Mohseni has served on many international conference committees, scientific review panels, and editorial boards. He has published over 260 articles in major journals including Nature and Nature Photonics. Mohseni has been involved in several startups as founder and CTO. He holds 35 issued US and International patents and patent applications. He is a Fellow of SPIE and OSA.

© 2023 The Authors. Small Methods published by Wiley-VCH GmbH

23669608, 0, Downloaded from https://onlinelibrary.wiley.com/doi/10.1002/smtd.202300595 by Northwestern University Libraries, Wiley Online Library on [14/11/2023]. See the Terms and Conditions (https://onlinelibrary.wiley.com/terms-and-conditions) on Wiley Online Library for rules of use; OA articles are governed by the applicable Creative Commons License